

UC Berkeley

UC Berkeley Electronic Theses and Dissertations

Title

Relaxation in Magnetic Particle Imaging

Permalink

<https://escholarship.org/uc/item/4tm8n7kh>

Author

Croft, Laura Rose

Publication Date

2013

Peer reviewed|Thesis/dissertation

Relaxation in Magnetic Particle Imaging

by

Laura Rose Croft

A dissertation submitted in partial satisfaction of the

requirements for the degree of

Joint Doctor of Philosophy
with University of California, San Francisco

in

Bioengineering

in the

Graduate Division

of the

University of California, Berkeley

Committee in charge:

Professor Steven Conolly, chair

Professor John Kurhanewicz

Professor John Clarke

Fall 2013

Abstract

Relaxation in Magnetic Particle Imaging

by

Laura Rose Croft

Joint Doctor of Philosophy in Bioengineering
with University of California, San Francisco

and

University of California, Berkeley

Professor Steven Conolly, Chair

Magnetic particle imaging (MPI) is a novel medical imaging modality that spatially detects a tracer of superparamagnetic iron oxide nanoparticles (SPIOs) with high sensitivity, contrast, and no tissue penetration limitations. MPI has great potential for safer angiography, *in vivo* cell tracking, and cancer detection, among other applications. Current MPI theoretical descriptions and reconstruction techniques make an *adiabatic* assumption that the SPIO tracer instantaneously follows the applied magnetic fields of the MPI scanner. This assumption is not strictly true, and we refer to SPIO magnetization delays as *relaxation* effects.

We begin by extending the x-space theory of MPI to include relaxation effects. We choose this MPI theory because it directly converts the temporal MPI signal to the image (spatial) domain, lending itself well to investigating how relaxation time delays translate into spatial effects. Using the non-adiabatic x-space theory and experimentally-measured data, we demonstrate that relaxation blurs the x-space image in the scanning direction.

Next, we study how we may design MPI scanning sequences to minimize relaxation-induced blurring. From the non-adiabatic x-space theory we derive a mathematical description of how this blur can vary with scanning parameters for a given relaxation time. We compare theoretical predictions to experimental data by measuring relaxation times and spatial resolution under various scanning conditions. Despite increased relaxation time delays with slower scanning conditions, we observe that relaxation-induced blurring can be minimized when scanning slower.

Finally, we derive a magnetic field-driven relaxation mechanism called *magneto-viscous* relaxation. This mechanism describes how the applied magnetic field creates a magnetic torque on the SPIO, inducing physical rotation of the SPIO to align with the field; however viscous resistance of the carrier liquid hinders this movement. We compare predicted relaxation times to measured values for a range of SPIO characteristics and scanning conditions.

In this dissertation, we show how relaxation can have deleterious effects on the MPI signal and image. We explore how relaxation-induced blurring and relaxation times may be minimized through improved SPIO characteristics and MPI scanning sequence design. In addition to improving MPI image quality, this important area of research can lead to future clinical applications. Using this knowledge and specially-designed MPI pulse sequences, we can exploit variations in relaxation behavior as a source of contrast, which will increase the diagnostic potential of MPI.

To my family & friends

Acknowledgments

I have been very fortunate to meet many wonderful people throughout my graduate school experience. These people have enriched my life, and I would like to take this opportunity to thank them.

First, I would like to thank my advisor, Steven Conolly. Finding someone who will teach you is one of the most valuable things in life, and I would not have been able to achieve this work without his guidance and his ability to challenge me to be a better engineer, theorist, presenter, and writer. Steve is also a special type of person who will take the time to talk to any student, giving advice when it is needed or simply lending an ear. Steve helped me immensely even before I joined the lab, and I think he has a unique gift for helping students to focus on and identify what it is that they really want out of graduate school, a first job, their career, and their lives. He has been a “life coach” if you will to many students who have faced a tough decision or dilemma in their time here at Berkeley, and I have been very fortunate to have him as my research mentor as well.

The next two people I would like to thank are two more examples of great teachers, Patrick Goodwill and Emine Saritas. Patrick has challenged and helped improve my hardware and software engineering skills, and the outcome has been the relaxometer set-up and data in this work. His vision for MPI is inspiring, and I count myself lucky to have learned from such a superstar. Emine has been a great mentor in the lab as well. She has given me valuable advice about experiments, writing, and different cultures, and she always impresses me with her patience and her ability to listen. She has been a great emotional support in the lab as well, and I know that she will be an amazing professor next year!

During my time at an internship, I realized that I have been so lucky to spend my days at Berkeley working with friends. I would like to thank Gary Lee, Kuan Lu, Bo Zheng, and Justin Konkle for being my friends as well as colleagues. One of the best things about our lab is how collaborative it is, and each of these people have taken significant time out of their days to help me, be it to build a filter, to run a MPI scan, or to find that pesky bug in the Matlab code. I would also like to thank the wonderful undergraduate students that I have worked with: Arbi Tamrazian, Daniel Price, Eric Chu, Ada Li, and Wisely Yang. They have been great assistants and pleasant company during long experiments. I would also like to thank my collaborators: Matt Ferguson, Hamed Arami, Amit Khandar, and Kannan Krishnan at the University of Washington, and Laurie Drews and Matthew Tirrell here at UC-Berkeley. My work studying nanoparticle behavior and its effect on imaging would not be possible without this outside assistance on supplying, characterizing, and modifying many of the particles that I study.

I would like to thank my dissertation committee, John Kurhanewicz (UCSF) and John

Clarke (Berkeley), for their time, help, and encouragement. I would also like to thank the members of the Berkeley Bioengineering staff, and in particular, Rebecca Pauling. Rebecca has always been available to listen to a problem or to just have a great conversation and laugh. She is truly an advocate for the students and has been a very important source of support for me personally throughout my BEAST activities and research decisions.

My time in graduate school would not have been the same without my friends. There are too many wonderful people to name, but in particular, I would like to thank Maral Gharib, Monica Kapil, Sophie Wong, Jeff Henry, Anuj Patel, Rick Henrikson, Tim Downing, and Emma Essock-Burns for their support throughout the years. Thank you for all the advice, listening ears, laughs, and fun times. I would also like to thank my east coast support system: Carly Westcott, Lindsey Thompson, Shilpa Arya, Lindsey Blaise, Mary Winn Miller, and Kendra Kofler. With each visit with my girls, they refresh my spirits and motivate me to get my act in gear when I returned to school.

Last but not least, I would like to thank my parents, Steve and Janet Croft. None of my accomplishments would have been possible without them. Thank you for all the love and support and for always believing in me.

Contents

1	Background	1
1.1	Magnetic Particle Imaging (MPI)	1
1.1.1	Introduction to Magnetic Particle Imaging	1
1.1.2	Superparamagnetic Iron Oxide Nanoparticles (SPIOs)	1
1.1.3	Magnetic Particle Imaging Applications	3
1.1.3.1	Angiography	4
1.1.3.2	<i>In vivo</i> Stem Cell Tracking	4
1.1.3.3	Cancer Detection	5
1.1.3.4	Atherosclerotic Plaque Detection	5
1.1.4	MPI Systems Theory & Reconstruction	5
1.2	Relaxation Effects	6
1.2.1	Thermal-Driven Relaxation Mechanisms	6
1.2.1.1	Néel Relaxation Mechanism	7
1.2.1.2	Brownian Relaxation Mechanism	7
1.2.1.3	Relaxation Mechanisms Act in Parallel	7
1.2.2	Magnetic Field-Dependent Relaxation	8
1.2.3	MPI Relaxation	9
2	Relaxation in X-Space Magnetic Particle Imaging	10
2.1	Introduction	10
2.2	Theory	11
2.2.1	Review of Adiabatic X-Space Theory in One Dimension	11
2.2.2	Non-Adiabatic X-Space Theory in One Dimension	12
2.3	Methods	14
2.3.1	Berkeley X-Space Projection MPI scanner	14
2.3.2	Berkeley X-Space Relaxometer	14
2.3.3	Theoretical Calculations	15
2.3.4	Fitting Algorithm for Relaxation Time Measurements	15
2.4	Results	16
2.4.1	Relaxation Blurs the X-Space Image in the Scanning Direction	16
2.4.2	MPI X-Space Theory with Relaxation Predicts Point Spread Function	17
2.4.2.1	Berkeley X-Space Projection MPI scanner	17
2.4.2.2	Berkeley X-Space Relaxometer	17
2.4.3	MPI X-Space Theory with Relaxation Predicts Experimental Images	17
2.5	Discussion	18

2.6	Conclusions	19
3	Effects of Drive Field on Relaxation-Induced Blurring in Magnetic Particle Imaging	22
3.1	Introduction	22
3.2	Theory	23
3.2.1	Review of Non-Adiabatic X-Space Theory for MPI	23
3.2.2	Linear Approximation for Sinusoidal Drive Fields	24
3.2.3	Relaxation in the Spatial Domain	24
3.3	Methods	26
3.3.1	Berkeley 3D MPI Scanner	26
3.3.2	Berkeley Relaxometer	27
3.3.3	Partial FOV Scanning to Measure Spatial Resolution	28
3.3.4	Fitting Algorithm to Measure Relaxation Times	30
3.4	Results	31
3.5	Discussion	32
3.6	Conclusions	34
3.7	Appendix	34
4	Magneto-Viscous Relaxation in Magnetic Particle Imaging	36
4.1	Introduction	36
4.2	Magneto-Viscous Relaxation Theory	37
4.2.1	Dynamic Langevin Equation	37
4.2.2	Magneto-Viscous Relaxation Time Constant	39
4.3	Methods	40
4.3.1	Berkeley X-Space Relaxometer	40
4.3.2	Linear Approximation for the Time-varying Drive Field	40
4.3.3	Experimental Relaxation Time Measurements	40
4.3.3.1	Fitting Algorithm	40
4.3.3.2	Non-Adiabatic X-Space Theoretical Calculations	41
4.3.4	Magneto-Viscous Relaxation Time Theoretical Calculations	41
4.4	Results	43
4.4.1	Relaxation Times Decrease with amplitude of Magnetic Torque	43
4.4.1.1	Relaxation with Magnetic Slew Rate	43
4.4.1.2	Relaxation with Magnetic Size	43
4.4.2	Relaxation Times Increase with Viscous Resistance	43
4.5	Discussion	44
4.6	Conclusions	45
4.7	Appendix	46
5	Future Directions	50
5.1	Biosensor Applications	50
5.2	Relaxation-Based Contrast in MPI	50
5.2.1	Preliminary MPI Relaxation-Based Contrast Imaging	51
5.2.2	Relaxation-Based Contrast Applications	52

5.2.2.1	Targeted Cancer or Atherosclerotic Plaque Detection	52
5.2.2.2	Visualizing SPIO Uptake at Inflammation Sites	53
5.2.2.3	Cell Death Monitoring for MPI Cell Tracking	53
6	Conclusions	55

List of Figures

1.1	The net magnetization (M) of an ensemble of SPIOs follows the Langevin function of paramagnetism in response to an applied magnetic field (H). The H field, when positive, points to the right in this figure.	3
1.2	Since relaxation mechanisms act in parallel, the effective relaxation time is equal to whichever mechanism is fastest at a given particle size. Néel, Brownian, and effective relaxation times all increase with particle size.	8
2.1	Adiabatic x-space scanning blurs the SPIO density input according to the Langevin magnetization of the SPIOs. Relaxation effects further blur the image and create an asymmetrical shape to the PSF. This blurring effect occurs in the scanning direction, which results in non-identical PSFs for the two scanning directions. ©2012 IEEE	12
2.2	The Berkeley x-space projection MPI scanner (a) acquires two-dimensional images. A 2.3 T/m magnetic gradient creates a field-free-line (FFL), and the drive coil scans this FFL at 22.9 kHz with field strengths up to 35 mT-pp. The Berkeley x-space relaxometer, shown with side (b) and top (c) views, measures the point spread function of a particle sample. The drive coil generates a sinusoidal magnetic field of 10-200 mT-pp strength at frequencies of 1.5-11.5 kHz. The signal received from the gradiometric receive coil is digitized at 10 MSPS without filtering. The bias coil can add ± 180 mT field for partial field of view scanning.	16
2.3	Experimentally-measured PSFs displayed alongside theoretical PSFs calculated from the adiabatic and the non-adiabatic x-space theory for each scanning direction. The inclusion of relaxation into the theory predicted a significant loss in predicted resolution and peak signal and produced a shape which more closely resembled that of the experimental signal. (a,b) We compared the x-space theoretical PSFs to a one-dimensional profile through (inset) a positive-velocity scan image of $2 \mu L$ of undiluted Resovist acquired in the projection MPI scanner with a drive field of 20 mT-pp at 22.9 kHz. (c,d) We measured a PSF of Resovist in the relaxometer with a drive field of 60 mT-pp at 4.4 kHz. ©2012 IEEE	20

2.4	(a) A line resolution phantom was constructed with 1.75 mm wide wells which were filled with 20x diluted Resovist. We acquired (b) a positive-velocity scan image of this phantom in the projection MPI scanner at 20 mT-pp. We visualized a one-dimensional profile through the center of this image and compared this profile to the image predicted by (c) the adiabatic x-space theory and by (d) the non-adiabatic x-space theory. The experimentally-measured image showed better agreement with the non-adiabatic x-space theory than with the adiabatic x-space theory. ©2012 IEEE	21
3.1	The adiabatic point spread function (PSF) is spatially convolved with a relaxation term $r\left(\frac{x}{v_s}\right)$, which blurs the image in the scanning direction. Relaxation-induced blurring, Δx_{relax} , increases with increasing relaxation time τ and with increasing drive field scanning rate v_s via either frequency or amplitude. . . .	23
3.2	(a) The Berkeley 3D MPI scanner acquires three-dimensional images using a 7 T/m selection field. A drive coil scans the FFP of the scanner at 23.2 kHz at peak amplitudes up to 30 mT. The Berkeley relaxometer, shown with (b) side and (c) top views, measures the point spread functions (PSF) of SPIO nanoparticles. A sinusoidal magnetic field is generated in the drive coil at frequencies of 1.5-25 kHz and of 5-100 mT drive field peak amplitude. The MPI signal is acquired in a gradiometer receive coil through induction at 10 MSPS without filtering. The bias coil produces up to a ± 180 mT field. . . .	26
3.3	Transmission electron microscopy (TEM) images of two SPIO nanoparticle tracers: (a) Resovist (Bayer-Schering, Berlin, Germany), and (b) UW33, which was synthesized at the University of Washington.	27
3.4	Example of a point spread function (PSF) of Resovist measured in the relaxometer using the partial field-of-view (FOV) method at a drive field of 30 mT peak amplitude at 9.3 kHz. Multiple partial FOVs were scanned while the bias coil applied a linear ramp from -75 mT to +75 mT. The partial FOVs, each shown as a different color in (a), were merged to form the unstitched PSF. Next, the partial FOVs were averaged to form (b) the stitched PSF, which compares well to the non-adiabatic theoretical PSF (calculated with a 2.3 μ s relaxation time). The adiabatic theory predicts a more symmetric PSF with less blur, which does not capture the effects of relaxation.	28

3.5	(a) Spatial resolution of (d) a point source of undiluted Resovist nanoparticles ($2 \mu\text{L}$) deteriorated as the 3D MPI scanner drive field amplitude increased and was comparable to resolution measured in the relaxometer at a similar frequency (23.2 kHz for the MPI scanner vs. 25 kHz for the relaxometer). Resolution was measured as the full-width at half maximum (FWHM) width of (c) the 1D profile in the z direction through the center of (b) the image in the xz-plane. The reported value is the average of the negative- and positive-velocity scan images. Here, only the positive-velocity image is displayed. Scan time was 2 minutes 52 seconds for a FOV of 2 cm x 2 cm x 4.8 cm. Relaxometer-measured resolution was converted to units of space using the same magnetic field gradient (3.5 T/m in the z direction) as the MPI scanner.	29
3.6	Relaxometer-measured resolution for (a) Resovist and (b) UW33 deteriorated with increasing drive field amplitude, and showed relatively modest changes with frequency. Resovist experiences more resolution deterioration than UW33 with increasing drive field amplitude. Theoretical predictions of resolution (solid lines) calculated from average phase lags showed comparable values to measured resolution (shapes). Resolution was measured as the full-width at half maximum (FWHM) widths of point spread functions (PSFs) acquired in the relaxometer using partial field-of-view methods. Error bars indicate the standard deviation from the average value for three sets of data.	30
3.7	Relaxation times of (a) Resovist and (b) UW33 measured in the relaxometer decreased with increasing magnetic slew rate, which was varied by increasing both drive field amplitude (5-30 mT) and frequency (4.5, 9.3, 12.2, and 25 kHz). While relaxation times showed greater decreases with field amplitude at the lower frequencies, (c) phase lags were comparable across the tested range of frequencies. Measured relaxation times were translated to phase lags by multiplying by 2π and the drive field frequency. The phase lags averaged across the four frequencies are displayed as the solid lines in (c).	31
3.8	(a) Peak signal increased linearly with drive field amplitude for point sources of Resovist measured in the 3D MPI scanner and in the relaxometer at 23 kHz and 25 kHz, respectively. These values were normalized to the peak signal of the 27.6 mT data for comparison. Peak signal increased linearly with magnetic slew rate, increased via drive field amplitude and frequency, for (b) Resovist and (c) UW33 measured in the relaxometer at 4 frequencies (4.5, 9.3, 12.2, and 25 kHz) at a range of 5-30 mT amplitude. The peak signals in (b) and (c) were normalized to the peak signal acquired at the highest magnetic slew rate, 4710 T/s.	32
4.1	SPIO magnetic dipole moment orientation under varying influences where the angle of the magnetic dipole moment $\theta(t)$ and the applied magnetic field $H(t)$ are defined in reference to the x-axis. The applied magnetic field creates a torque on the magnetic dipole moment of the nanoparticle, thermal motion promotes random rotations, and the viscosity of the carrier liquid exerts a resistance against both these motions.	38

4.2	Transmission electron microscopy (TEM) images of the SPIO nanoparticle tracers: Resovist and three samples of varying magnetic and hydrodynamic sizes (UW20-A, UW20-B, and UW23) synthesized at the University of Washington.	47
4.3	Measured relaxation times for Resovist (A) and UW20-A (B) decreased with increasing magnetic slew rate. Relaxation times were acquired in the Berkeley x-space relaxometer at five frequencies (2.3, 4.5, 9.3, 12.2, and 25 kHz) for drive field amplitudes in the range of 15-70 mT. The measured relaxation times compared well with the theoretical values predicted by magneto-viscous relaxation across the range of measured magnetic slew rates.	48
4.4	Measured and theoretical relaxation times for UW20-A are compared to those for a sample with a larger magnetic size (UW23) and and a larger hydrodynamic size (UW20-B). (A) The SPIO sample with a larger magnetic core, UW23, had shorter relaxation times as compared to those of UW20-A, as predicted by magneto-viscous relaxation theoretical calculations. (B) The UW20-B sample had greater relaxation times than UW20-A as predicted by the magneto-viscous relaxation predictions. Experimentally-measured relaxation times were acquired in the Berkeley x-space relaxometer at three frequencies (4.4, 9.1, and 11.5 kHz); the average and standard deviation between the three frequencies are displayed at each magnetic slew rate.	49
5.1	Illustration of (a) a functionalized SPIO biosensor and its target, which can form (b) an assembly of multiple SPIOs and targets. Relaxation times would increase as the assembly grows larger with increased concentrations of the targeted molecule.	51
5.2	The first relaxation-based contrast MPI image distinguishes the SPIOs with longer relaxation times (Resovist); whereas those with short relaxation times (Chemicell) are only seen in the native x-space MPI image.	52
5.3	Sources of relaxation-based contrast for MPI	53
5.4	Illustrations of (b) a standard MPI image and (c) a relaxation-based contrast image to detect (a) plaque present in the carotid artery. Note that these images are merely illustrations of a concept and are not from data.	54

List of Tables

4.1	Magnetic core diameter distributions (mean \pm standard deviation) as measured by transmission electron microscopy (TEM), the magnetic core diameter distributions used in the theoretical calculations of magneto-viscous relaxation times, hydrodynamic diameters as measured by dynamic light scattering (DLS), and the hydrodynamic diameter values used in theoretical calculations of magneto-viscous relaxation times.	42
-----	---	----

Chapter 1

Background

1.1 Magnetic Particle Imaging (MPI)

1.1.1 Introduction to Magnetic Particle Imaging

Magnetic particle imaging (MPI) is a new medical imaging modality first published by Philips Research in 2005 [1, 2]. This novel type of scanner exploits the nonlinear magnetization response of superparamagnetic iron oxide nanoparticles (SPIOs) to generate a positive contrast image of this safe tracer with excellent sensitivity, contrast, depth penetration, acquisition time, and without using ionizing radiation.

MPI scanners use a strong magnetic gradient, called a selection field, to create a region of zero field, or field-free-point (FFP). Alternatively, selection fields can be designed to create a field-free-line (FFL) for acquiring two-dimensional projection images [3, 4]. As a time-varying homogenous drive field scans the FFP or FFL across an SPIO, the magnetic dipole moment of the SPIO will reorient. This SPIO “flip” changes the direction of magnetization, which is inductively detected by a receiver coil. By correlating the time trajectory of the FFP with the SPIO responses received, one can reconstruct an image with intensity linear to the SPIO mass located at the FFP or FFL. MPI scanning does not elicit a response from tissue, so only the tracer of SPIOs is visualized in the image, providing for extraordinary contrast. The sensitivity and spatial resolution of MPI is intrinsically related to the quality of the SPIO tracer; therefore the success of MPI is inextricably linked to the development of tailored MPI tracers.

1.1.2 Superparamagnetic Iron Oxide Nanoparticles (SPIOs)

MPI directly measures the location and concentration of a tracer of SPIOs. SPIO imaging agents were originally developed as MR contrast agents. These agents caused T_2^* dephasing effects, providing negative contrast, or hypointensity, in the region of tissue immediately surrounding the SPIO tracers. These agents can be intravenously or orally delivered and can even be used to tag cells to be injected. Many of these MR agents were introduced to the market several years ago, but nearly all have been discontinued due to insufficient revenues. The most commonly used SPIO agent for MPI has been Resovist (Bayer-Schering, Berlin, Germany), which was an MR agent for diagnosing liver cancer [5]. Recently new tracers

under development for pre-clinical MRI (Micromod GmbH, nanoPET Pharma GmbH [6, 7]) as well as for MPI specifically (University of Washington, LodeSpin Labs, LLC [8, 9]) show promising results in MPI.

SPIOs have an iron oxide core (magnetite or maghemite) with a polymer coating to prevent aggregation and to allow suspension. SPIOs are single-domain, which means that the size of the iron oxide cores is sufficiently small so that only one magnetic domain, and therefore magnetic dipole moment, exists within the magnetic material. The implication of being single-domain is that each iron oxide core is always fully magnetized to a single direction. As long as the iron oxide cores are sufficiently separated by their polymer coatings to prevent magnetic interactions, each magnetic dipole moment can orient independently within the liquid suspension. By gathering an ensemble of these nanoparticles, we obtain a material that behaves as a paramagnet, but can achieve much greater values of net magnetization, hence the term, *super*paramagnetism.

Illustrated in Figure 1.1, the Langevin function of paramagnetism describes the net magnetization M [A/m] of N [particles/ m^3] SPIOs in response to an applied magnetic field H [A/m] [10]:

$$M(H) = Nm\mathcal{L}\left[\frac{\mu_0mH}{k_B T}\right] \quad (1.1)$$

$$= Nm\left[\coth\left(\frac{\mu_0mH}{k_B T}\right) - \frac{k_B T}{\mu_0mH}\right] \quad (1.2)$$

where m [A·m²] is the magnetic moment of the SPIOs, $\mathcal{L}(\alpha) = \coth(\alpha) - 1/\alpha$ is the Langevin function, μ_0 is the vacuum permeability, k_B is Boltzmann's constant (1.38×10^{-23} J/K), and T [K] is the temperature. Note that the direction of M is parallel to H . As seen in Equation 1.1, the net magnetization is a function of the ratio of magnetic energy μ_0mH [J] to thermal energy $k_B T$ [J]. At zero applied magnetic field, thermal motion randomly orients each SPIO and is the only torque acting on the SPIOs. This dispersion of magnetic dipole moment orientations results in zero net magnetization of the ensemble. As the applied magnetic field increases and becomes increasingly large compared to thermal motion, an increasing number of SPIOs will align with the applied magnetic field. When the applied magnetic field is sufficiently strong enough, thermal motion becomes negligible, and all the SPIOs align with the applied field. This maximum net magnetization is referred to as the saturation magnetization.

SPIO magnetic moment increases with the size of the magnetic core: $m = M_{\text{sat}}V_m$ where V_m is the volume of the particle's magnetic core, and $M_{\text{sat}} = 0.6 \text{ T}/\mu_0$ for magnetite nanoparticles. As the size of the magnetic content of the particle increases, the magnetic energy term increases. Therefore with increasing magnetic core size, the Langevin curve becomes steeper and saturation magnetization is achieved at lower applied fields. Note that this M_{sat} differs from the saturation magnetization reached in Equation 1.1 in the sense that this is the magnetization inside the particle and is a property of the fixed density of magnetite. The saturation magnetization of Equation 1.1 is dependent on N [particles/ m^3] and therefore varies with particle concentration.

A primary advantage of SPIOs as a medical imaging agent is that they are safe for human use. They are not radioactive, unlike nuclear medicine agents, and are safe for weak kidneys,

unlike the iodine and gadolinium agents commonly used in CT and MRI. Many foreign bodies between 6-50 nm in diameter, such as iodine and gadolinium agents, are filtered from the bloodstream and excreted via the kidneys [9, 11]. Note that clearance mechanisms are also dependent on a molecule's charge and configuration, in addition to being heavily-determined by size. Many patients have weak kidneys due to chronic kidney disease (CKD), acute trauma, and other conditions which have damaged the kidneys' filtration abilities. In the case of CKD, patients exposed to iodine have a thirty percent risk of contrast-induced nephropathy (CIN), which triples mortality [12, 13], and patients administered gadolinium are at risk of nephrogenic systemic fibrosis [14]. SPIOs, which are greater than 50 nm diameter, are cleared from the bloodstream by the reticulo-endothelial system (RES) and are sequestered primarily in the liver before leaving the body [9, 15, 16]. Because SPIO agents avoid clearance through the kidneys, they are safer for patients with renal insufficiency, and in fact, an SPIO agent (Ferumoxytol, AMAG Pharmaceuticals, Lexington, MA) is even approved by the FDA as a treatment for iron deficiency anemia in CKD patients [17].

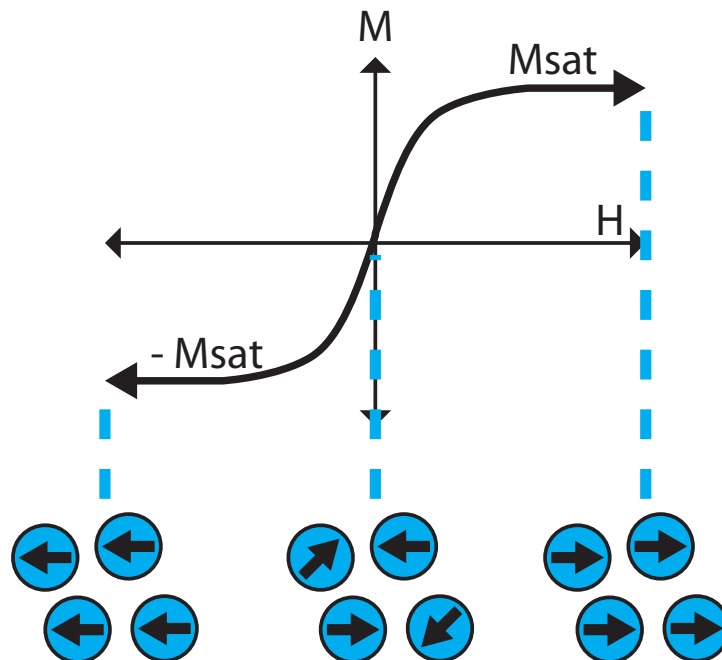


Figure 1.1: The net magnetization (M) of an ensemble of SPIOs follows the Langevin function of paramagnetism in response to an applied magnetic field (H). The H field, when positive, points to the right in this figure.

1.1.3 Magnetic Particle Imaging Applications

MPI is an exciting new imaging technique with a variety of possible applications, both clinical and pre-clinical.

1.1.3.1 Angiography

MPI shows great potential as a new angiography alternative that can non-invasively acquire three-dimensional, quantitative images of an SPIO-illuminated arterial tree. This image would be unobscured by human tissue, as it does not contribute to or attenuate the MPI signal. Diamagnetic human tissue has a weak ($\chi = -9 \times 10^{-6}$) magnetic susceptibility compared to magnetite ($\chi = 70$); therefore, the signal from human tissue is negligible compared to the SPIO response, even at low SPIO concentrations [18]. Moreover, in MPI we detect only the nonlinear response, which stems from the saturation behavior of the SPIOs. Diamagnetic materials do not saturate, therefore tissue produces zero nonlinear response, or in other words, no harmonics (see Section 1.1.4). Using a simple model for homogeneous muscle tissue, the penetration depth of MPI is estimated to be 6 meters, and may be even greater due to tissue heterogeneity [19, 20, 21]. Therefore, MPI provides extraordinary contrast and has no depth attenuation effects, characteristics that make MPI well-suited for angiographic applications. Additionally, MPI shows great promise to have sufficient sensitivity and contrast to use a venous injection, thereby avoiding the serious complications possible with catheterized arterial injections.

MPI angiography would be particularly advantageous for patients with chronic kidney disease (CKD). CKD patients comprise 25% of those that present to the angiography suite, and constitute 47% of the US population over age 70 [22, 23, 24]. As discussed in Section 1.1.2, SPIOs are much safer for vulnerable kidneys than the iodine and gadolinium agents used in X-ray, CT, and MR angiography, and additionally, MPI does not use ionizing radiation unlike X-ray and CT.

1.1.3.2 *In vivo* Stem Cell Tracking

Cellular therapies are under development to heal tissue damage associated with chronic disease including chronic heart failure [25], diabetes [26], and neurodegenerative diseases such as Parkinson’s disease or Alzheimer’s disease [27]. Imaging methods are needed to track the delivery and long term survival of these therapies in order to optimize the therapeutic benefit and protocol. Currently no ideal imaging modality exists for longitudinal *in vivo* cell tracking. For example, current modalities have limitations such as depth-dependent blurring and attenuation. Previously demonstrated using MRI, SPIOs can label stem cells, on the order of 10 pg/cell [28], which are then injected or transplanted into an animal for study. SPIO tagging in MRI appears hypointense (black) in the image, which makes it challenging to quantify the SPIO, or labeled cell, number. More recently, experimental work has demonstrated that MPI can image SPIO-labeled stem cells with positive, or hyperintense, contrast. Most importantly, the image intensity is linear and quantitative with iron content, from which we can quantify cell number [29]. *In vivo* cell tracking with MPI is also advantageous because it has high sensitivity and contrast, and does not suffer from any depth penetration limitations. In addition to stem cells, other tagging applications include tracking and studying the behavior of dendritic cells or cancer cells.

1.1.3.3 Cancer Detection

MPI could be used to diagnose cancer through both untargeted and targeted approaches. As seen in MRI, tumor sites may be identified by *enhanced dynamic permeability*, in which tracer injected into the bloodstream tends to accumulate in tumor tissue due to its “leaky” vasculature. This is referred to as the enhanced permeability and retention (EPR) effect of cancerous tissue [30]. Another passive means by which SPIOs may highlight tumor sites may be due to the tendency of phagocytic cells to ingest them. SPIO uptake has been demonstrated in cells such as macrophages and astrocytes located at the periphery of tumor sites, but has not been seen in actual tumor cells [31, 32]. A targeted approach can be pursued by functionalizing the SPIO surface with a targeting peptide or antibody. SPIOs functionalized with the CREKA peptide bind to clot formation present at tumor sites [33, 34], and SPIOs with variants of an RGD peptide target a specific integrin present on tumor cells [35]. Note that targeted MR agents must have the iron oxide agents on the surface of the particles (to interact with external water molecules); hence the targeting and the iron oxide labels compete for surface area. For MPI, we can decorate the entire surface of the nanoparticle with targeting agents with no need for the iron oxide to interact with the adjacent tissues.

1.1.3.4 Atherosclerotic Plaque Detection

Atherosclerotic plaque may also be identified using similar strategies as MPI for cancer detection. Inflammatory cells present at atherosclerotic plaques, such as macrophages, have been shown to phagocytose SPIOs [36, 37]. Targeted approaches to detect plaque are also similar to those for cancer. The CREKA peptide binds to fibrin-containing blood clots present at plaque formation [38], and RGD variants also bind to certain integrins present at atherosclerotic plaques [39].

1.1.4 MPI Systems Theory & Reconstruction

To compete with existing technologies for these imaging applications, MPI systems theory is essential to understand how to optimize spatial resolution, signal-to-noise ratio (SNR), contrast, hardware and safety concerns. Unlike MRI, which also uses magnetic fields to acquire images, MPI simultaneously transmits and receives signals via inductive electromagnetic coils. While this endows MPI with the potential to acquire images faster than MRI methods, it presents the problem of signal contamination. The signal received in the MPI scanner will include the drive field as well as the SPIO response. Since the signal from the drive field is much greater than the SPIO signal, we must try to eliminate it while maintaining as much of the SPIO signal as possible. The drive field is typically a sinusoidal field at some frequency f_0 . When we view the SPIO response in the temporal frequency domain, we see that its spectrum contains content only at harmonics of f_0 (including f_0). The primary approach to discard drive field content is to filter out the fundamental frequency f_0 and retain only the higher harmonic content from the SPIO signal. However, this filtering also eliminates any SPIO signal content in the filtered frequency band, which presents a challenge when interpreting the filtered signal in the temporal domain.

The standard systems theory approach by Philips models MPI in the temporal frequency domain and reconstructs the image from the harmonics of the SPIO signal. By measuring the received harmonic spectrum of a point source at each position in the field-of-view (FOV), a pre-characterization is performed to acquire what is known as a *system matrix* [1, 40]. Image reconstruction requires multiplying by the inverse of the large system matrix. The advantage of this approach is that it does not require recovering the lost SPIO information; however the inversion of the system matrix is often not well-conditioned and typically requires regularization or iterative methods. Moreover, this reconstruction method may be too complex for real-time reconstruction.

The newer x-space theory views MPI as a scanning process in the image domain [41, 42]. Spatial localization is performed by using the known FFP trajectory to translate the MPI temporal signal to the spatial domain. Deconvolution to improve image quality is an optional post-processing step that may incur a noise gain. This is a significant difference from system matrix methods in which spatial localization and deconvolution are coupled together in the same step. X-space reconstruction does necessitate recovering the lost SPIO information; however, this can be accomplished via a robust algorithm developed in [43]. Using this method, x-space reconstruction has demonstrated linearity and shift-invariance with essentially zero noise gain. Additionally, x-space reconstruction shows promise for real-time reconstruction since it requires only a point-division by the FFP velocity [3, 41, 42, 44].

1.2 Relaxation Effects

Both MPI system theories were derived under an *adiabatic* assumption that SPIO magnetization instantaneously follows the applied drive field. This applied magnetic field creates a torque on the magnetic dipole moments of the SPIOs and induces the SPIO alignment with that field. However, the orientation of the SPIO dipole moments are also influenced by other factors such as thermal fluctuations and viscous resistance to rotation. The competition of these torques causes a phenomenon known as relaxation, which delays the magnetization response of SPIOs. Relaxation descriptions for particle magnetization have been studied primarily for thermal processes, while a few studies have examined relaxation delays in the presence of an applied magnetic field.

1.2.1 Thermal-Driven Relaxation Mechanisms

Relaxation mechanisms based on thermal processes, Néel and Brownian relaxation, have been extensively studied in ferrofluid literature [45, 46]. Typically these mechanisms are used to describe cases in which an acting magnetic field has just been removed. Néel and Brownian relaxation time constants characterize the decay of the net magnetization of an ensemble of SPIOs after the field has been removed. Thermal motion randomly disperses the SPIO magnetic dipole moments from their previously aligned state, and this reorientation can occur via two mechanisms: the magnetic dipole moment rotates within the iron oxide core or the entire particle physically rotates.

1.2.1.1 Néel Relaxation Mechanism

Néel relaxation describes the former mechanism in which the magnetic dipole moment reorients within the magnetic material. The relaxation time constant can be calculated as:

$$\tau_N = \tau_0 \frac{e^\rho}{\sqrt{\rho}} \quad (1.3)$$

where

$$\rho = \frac{KV_m}{k_B T} \quad (1.4)$$

where τ_0 is a constant (10^{-9} s), K [J/m³] is the anisotropic energy constant, and V_m [m³] is the volume of the magnetic core of the nanoparticle [46, 47, 48]. The Néel relaxation time represents the ability of thermal energy ($k_B T$) to overcome the energy required for the magnetic dipole moment to rotate (KV_m). For larger nanoparticles, this energy barrier term is so high compared to thermal energy that the dipole moments are considered locked within the magnetic material, and Néel relaxation is energetically unfavorable. Another version of the Néel relaxation time constant allows for the inclusion of a *constant* applied magnetic field [47, 49, 50, 51]:

$$\tau_N = \tau_0 \exp \left[\frac{KV_m}{k_B T} \left(1 - \frac{H}{H_k} \right)^2 \right] \quad (1.5)$$

where $H_K = 2K/\mu_0 M_{\text{sat}}$. H_K [A/m] is the uniaxial anisotropy field that acts to resist the magnetic dipole moment from pointing in any other direction other than the preferred direction of the material. Typically in ferrofluid and MPI literature, the former, zero field calculation of Néel relaxation is used.

1.2.1.2 Brownian Relaxation Mechanism

Nanoparticles with locked dipole moments must physically rotate via Brownian relaxation, whose time constant is described by:

$$\tau_B = \frac{3\eta V_h}{k_B T} \quad (1.6)$$

where V_h [m³] is the hydrodynamic volume of the nanoparticle, and η [kg/(m·s)] is the viscosity of the carrier liquid [46, 52]. Hydrodynamic size is greater than magnetic core size as it includes the polymer coating of the SPIO. The Brownian relaxation time constant is the ratio of rotational hydrodynamic resistance ($6\eta V_h$) [J·s] to twice the thermal energy ($2k_B T$) [J], representing the ability of thermal motion to rotate the nanoparticle against the resistance of the carrier liquid.

1.2.1.3 Relaxation Mechanisms Act in Parallel

For unlocked nanoparticles, both relaxation mechanisms occur simultaneously, so the dominant relaxation mechanism is the faster mechanism for that nanoparticle's size and characteristics. The effective relaxation time constant of the two mechanisms in parallel is given by:

$$\tau_{EFF} = \frac{\tau_N \tau_B}{\tau_N + \tau_B} \quad (1.7)$$

Figure 1.2 gives an example of the effective relaxation time, Néel relaxation time, and Brownian relaxation time as a function of particle size for a particle with a 10 nm coating thickness and 20 kJ/m³ anisotropic constant, typical values for SPIOs used in MPI [8]. Néel relaxation is the faster mechanism for the smaller particles, whereas Brownian relaxation is the dominant mechanism for the larger particles. When the two mechanisms have comparable relaxation times, the effective relaxation time is faster than either mechanism alone as both mechanisms are contributing.

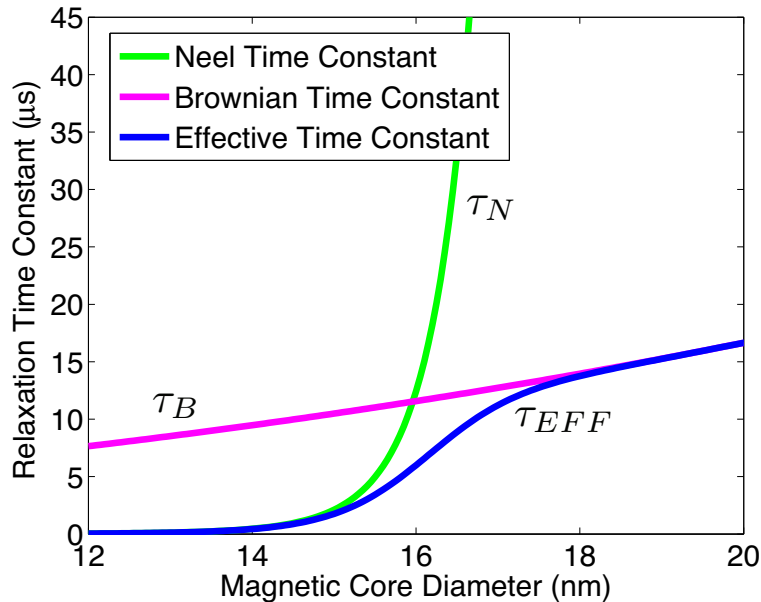


Figure 1.2: Since relaxation mechanisms act in parallel, the effective relaxation time is equal to whichever mechanism is fastest at a given particle size. Néel, Brownian, and effective relaxation times all increase with particle size.

Both of these relaxation times reflect the time delay of net magnetization dispersion as caused by random thermal motion. In these cases where the acting magnetic field has been turned off, only thermal motion is driving dipole orientation. However in MPI, the drive field continues to excite the SPIOs at the same time as the received signal detects their response.

1.2.2 Magnetic Field-Dependent Relaxation

Néel and Brownian relaxation mechanisms predict a time constant that is dependent primarily on temperature and particle size. It is perhaps not surprising that Brownian and the simpler form of Néel do not provide a perfect model of MPI relaxation, because they both assume that the magnetic field is zero. However, this is not really true in an MPI scan. In cases where a strong external magnetic field is present, theoretical derivations have predicted relaxation times or phase delays which are dependent on the parameters of the magnetic field,

such as field strength or frequency in the case of an AC magnetic field [46, 49, 53, 54, 55, 56]. One study derived a field-dependent, Brownian-like relaxation mechanism from the Fokker-Planck equation using numerical simulation [55]. Experimental investigations of magnetic nanoparticles demonstrated that relaxation times and phase delays decrease as an applied magnetic field increases in strength [49, 54, 57, 58]. Indeed, full Fokker-Planck differential equations describing the rotational motion of an ensemble of SPIOs contain external magnetic field terms which may easily dominate over thermal terms [59, 60, 61, 62].

1.2.3 MPI Relaxation

The dominant relaxation mechanism in MPI is still uncertain and will likely vary with particle characteristics, scanning sequences, and environmental conditions. MPI experimental studies have demonstrated that SPIO behavior can be affected by particle size [57], drive field parameters [57, 63], temperature [57, 64], and environmental viscosity [65, 66]. Comprehensive models of non-adiabatic MPI magnetization have been derived [61]; however these models require numerical methods to solve. Studies indicate relaxation properties of SPIOs may diminish MPI signal [8, 67], but to date, relaxation artifacts on reconstructed MPI scans have not been analyzed.

Here we investigate how relaxation affects the MPI image, and how we may modulate the resulting image artifacts or the MPI relaxation mechanism responsible for these effects. Using this information, we develop simple models to describe and predict the non-adiabatic MPI signal and image, the extent of image artifacts, and the MPI relaxation mechanism.

Chapter 2

Relaxation in X-Space Magnetic Particle Imaging¹

Magnetic particle imaging (MPI) is a new imaging modality that non-invasively images the spatial distribution of superparamagnetic iron oxide nanoparticles (SPIOs). MPI has demonstrated high contrast and zero attenuation with depth, and MPI promises superior safety compared to current angiography methods, X-ray, CT, and MRI angiography. Nanoparticle relaxation can delay the SPIO magnetization, and in this work we investigate the open problem of the role relaxation plays in MPI scanning and its effect on the image. We begin by amending the x-space theory of MPI to include nanoparticle relaxation effects. We then validate the amended theory with experiments from a Berkeley x-space relaxometer and a Berkeley x-space projection MPI scanner. Our theory and experimental data indicate that relaxation reduces SNR and asymmetrically blurs the image in the scanning direction. While relaxation effects can have deleterious effects on the MPI scan, we show theoretically and experimentally that x-space reconstruction remains robust in the presence of relaxation. Furthermore, the role of relaxation in x-space theory provides guidance as we develop methods to minimize relaxation-induced blurring. This will be an important future area of research for the MPI community.

2.1 Introduction

In this work, we amend the one-dimensional x-space theory to account for non-adiabatic SPIO magnetization. We show that the inclusion of relaxation effects is essential for theoretical predications to agree with experimental MPI data. We demonstrate theoretically and experimentally how relaxation blurs the x-space image and deteriorates resolution and SNR in the scanning direction. In a broader context, a simple model of relaxation will enable us to understand how to design MPI scanning to minimize blurring from relaxation and to achieve a desirable image resolution and signal strength. A better understanding of relaxation effects will benefit *both* x-space and harmonic reconstruction methods.

¹Excerpts of this chapter are from Croft, et al., Relaxation in x-space magnetic particle imaging, IEEE Transactions on Medical Imaging ©2012 IEEE.

2.2 Theory

2.2.1 Review of Adiabatic X-Space Theory in One Dimension

The x-space theory characterizes MPI as a scanning process in the image domain [41, 42]. Here we review the one-dimensional case; for the three-dimensional case, please see [42]. Under the adiabatic assumption that relaxation effects are negligible, the scalar magnetization of a SPIO in response to an applied field $H(x, t)$ [A/m] obeys the Langevin equation for paramagnetism

$$M_{\text{adiab}}(x, t) = m\rho(x)\delta(y)\delta(z)\mathcal{L}\left[\frac{H(x, t)}{H_{\text{sat}}}\right] \quad (2.1)$$

where m [A·m²] is the magnetic moment of the SPIOs, $\rho(x)$ [particles/m] is the 1D SPIO density, $\mathcal{L}[\bullet]$ is the Langevin equation, and H_{sat} [A/m] measures how easily a SPIO saturates. If we specify $H(x, t) = G(x - x_s(t))$ where G [A/m²] is the magnetic field gradient and $x_s(t)$ [m] is the position of the FFP (i.e., $x_s(t) = -H_{\text{homogeneous}}(t)/G$), then the adiabatic signal can be computed via the reciprocity theorem (see [68])

$$s_{\text{adiab}}(t) = -\frac{d}{dt} \iiint B_1 M_{\text{adiab}}(x, t) dx dy dz \quad (2.2)$$

$$= \dot{x}_s(t) \gamma \left(\rho(x) * \dot{\mathcal{L}}\left[\frac{Gx}{H_{\text{sat}}}\right] \right) \Big| \quad (2.3)$$

where B_1 [T/A] is the sensitivity of the receive coil. Here we defined the scalar terms $\gamma \triangleq \frac{B_1 m G}{H_{\text{sat}}}$. Note that MPI signal is a spatial convolution evaluated at the instantaneous FFP location multiplied by the instantaneous FFP velocity $\dot{x}_s(t)$ [m/s].

We now derive the adiabatic *X-Space Image Reconstruction Equation* by simply dividing the received signal by the instantaneous FFP velocity and scalar terms γ to obtain:

$$\hat{\rho}_{\text{adiab}}(x_s(t)) = \frac{s_{\text{adiab}}(t)}{\gamma \dot{x}_s(t)} \quad (2.4)$$

where $\hat{\rho}_{\text{adiab}}(x_s(t))$ is the adiabatic x-space image. Computing Equation 2.4, we obtain the *Adiabatic X-Space Imaging Equation*:

$$\hat{\rho}_{\text{adiab}}(x_s(t)) = \rho(x) * h(x)|_{x=x_s(t)} \quad (2.5)$$

which is the 1D magnetic particle distribution convolved with the MPI 1D point spread function (PSF), which we can clearly identify from this equation to be the derivative of the Langevin equation: $h(x) = \dot{\mathcal{L}}\left[\frac{Gx}{H_{\text{sat}}}\right]$.

The x-space analysis describes MPI as sampling of a linear, space-invariant (LSI) system, with an input of the SPIO spatial distribution and an output of the native image of that SPIO distribution. The x-space image reconstruction algorithm is quick, robust, and produces no noise gain. The x-space theory was derived with three physical assumptions [41, 42]:

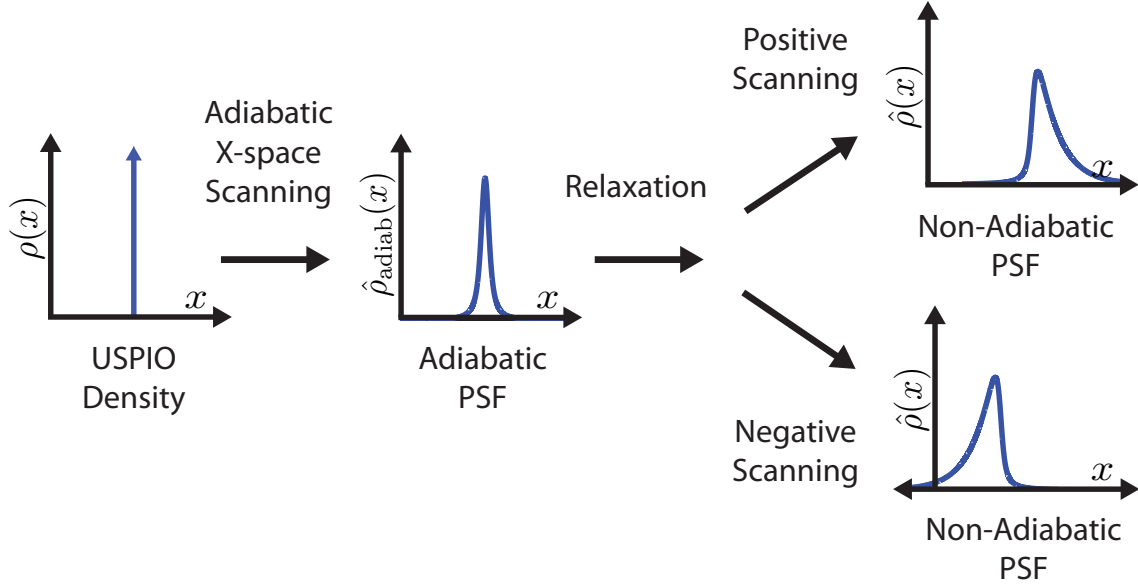


Figure 2.1: Adiabatic x-space scanning blurs the SPIO density input according to the Langevin magnetization of the SPIOs. Relaxation effects further blur the image and create an asymmetrical shape to the PSF. This blurring effect occurs in the scanning direction, which results in non-identical PSFs for the two scanning directions. ©2012 IEEE

1. The instantaneous FFP location is uniquely defined at every point in time. The unique FFP is guaranteed provided that the homogeneity of the gradient field and the FFP shifting field are adequately uniform over the imaging field-of-view (FOV). Even modest tolerances (about 20%) guarantee a unique FFP for 3D imaging MPI scanners.
2. First harmonic (the fundamental tone) information, which must be filtered out to avoid direct feedthrough contamination, is completely recoverable. Experimental proof that this lost first harmonic information is retrievable can be found in [42, 43, 44].
3. Rotation and alignment of the net magnetization of the SPIOs is adiabatic, or instantaneous, with the applied magnetic field. This assumption is not strictly valid. There have been studies on relaxation in MPI [61, 63] but to date no one has studied the effect of relaxation on image reconstruction or resolution.

2.2.2 Non-Adiabatic X-Space Theory in One Dimension

The well-established literature on ferrofluids typically models magnetic nanoparticle relaxation as a first-order Debye process. Hence, we adopted their first-order model to see if this model could predict our experimental findings in x-space MPI. One component of the Debye model is given by the differential equation [46, 52]

$$\frac{dM(x, t)}{dt} = -\frac{(M(x, t) - M_{\text{adiab}}(x, t))}{\tau} \quad (2.6)$$

where $M_{adiab}(x, t)$ [A/m] is the adiabatic magnetization, $M(x, t)$ [A/m] is the non-adiabatic magnetization, and τ [s] is the relaxation time constant. Solving this differential equation is straight forward, and one obtains this *temporal* convolution:

$$M(x, t) = M_{adiab}(x, t) * \frac{1}{\tau} \exp(-t/\tau) u(t) \quad (2.7)$$

for $\tau > 0$ where $u(t)$ is the Heaviside function. This result shows that SPIO magnetization can be approximated as a *temporal* convolution between an exponential relaxation term and the adiabatic magnetization. We can describe magnetization in a more general sense as a temporal convolution between the adiabatic magnetization and a convolution kernel $r(t)$ which represents the relaxation process:

$$M(x, t) = M_{adiab}(x, t) * r(t) \quad (2.8)$$

In this work, because we assume a Debye relaxation process, the relaxation term is an exponential decay, $r(t) = \frac{1}{\tau} \exp(-t/\tau) u(t)$. A common alternative would be a relaxation process modeled as a Gaussian decay. Additionally, the relaxation time constant, τ , could vary with nanoparticle size or other parameters, and there is always a distribution of nanoparticle sizes in any voxel. Hence, $r(t)$ could represent the sum of all the particles' relaxation processes; however in this work we use a single relaxation time constant τ . In any of these cases, the relaxation convolution breaks the adiabatic assumption made in the original x-space theory of MPI.

We combine Equations 2.1 and 2.8 to obtain

$$M(x, t) = m\rho(x)\delta(y)\delta(z)\mathcal{L} \left[\frac{H(x, t)}{H_{sat}} \right] * r(t) \quad (2.9)$$

as the full expression for non-adiabatic magnetization. To calculate the signal received by an inductive pick-up coil, we again use the principle of reciprocity. Evaluating the derivative using the convolution differentiation property $\frac{d(f*g)}{dt} = \frac{df}{dt} * g = f * \frac{dg}{dt}$ [69], we find that the resulting signal equation is a temporal convolution between the adiabatic signal and the relaxation convolution kernel:

$$s(t) = s_{adiab}(t) * r(t) \quad (2.10)$$

$$= \left(\dot{x}_s(t) \gamma \rho(x) * h(x)|_{x=x_s(t)} \right) * r(t) \quad (2.11)$$

Note that the first operation is a *spatial* convolution, whereas the second operation is a *temporal* convolution. Both convolutions can contribute to spatial blur in the reconstructed MPI image. However, they manifest very differently.

To reconstruct, we perform velocity compensation and gridding as performed in Equation 2.4. However, in this case velocity compensation imposes a challenge because now we cannot simply divide the signal by the FFP velocity. Therefore the non-adiabatic image reconstruction requires a modification. Because relaxation temporally delays the received signal, we estimate that the peak signal is delayed by approximately half the relaxation time. Therefore we modify the *Non-Adiabatic X-Space Image Reconstruction Equation* to read:

$$\hat{\rho}(x_s(t)) = \frac{s(t)}{\gamma \dot{x}_s(t - \frac{\tau}{2})} \quad (2.12)$$

Here we perform velocity compensation with the FFP velocity temporally delayed by half the relaxation time. Below we show that this approximation performs well in both simulations and experiments. The resulting image is approximated by the *Non-Adiabatic X-Space Imaging Equation*:

$$\hat{\rho}(x_s(t)) \approx \left(\rho(x) * h(x)|_{x=x_s(t)} \right) * r(t) \quad (2.13)$$

Again, we note this equation represents the SPIO density *spatially* convolved with the adiabatic PSF (the derivative of the Langevin equation), and now additionally *temporally* convolved with the relaxation term. Both convolutions blur the SPIO magnetization density, so both are critical to understanding and improving resolution and signal.

In Figure 2.1 we see that the addition of relaxation effects into the x-space theory causes an *asymmetric blur* based on scanning direction. With a sinusoidal drive field, the FFP oscillates back and forth in the *positive* and *negative* directions. With relaxation included, there is a visible alternation in the blur on alternating scanning directions. This asymmetry differs qualitatively from the adiabatic formulation in which the blur is completely symmetric regardless of scanning direction.

2.3 Methods

2.3.1 Berkeley X-Space Projection MPI scanner

The Berkeley x-space projection MPI scanner used to acquire images in this study scans with a FFL instead of a FFP (Figure 2.2a). The scanner has a 2.3 T/m main field gradient and a sinusoidal drive field operating at 22.9 kHz. Phase calibration was performed by using an SPIO sample (50 nm hydrodynamic diameter fluidMAG nanoparticles by Chemicell, Berlin, Germany) which experimentally demonstrated a negligible relaxation time. For more details on the Berkeley FFL scanner, refer to [3, 42]. For scanning, we laser cut an acrylic line resolution phantom with wells of 1.74 ± 0.10 mm thickness, as measured by micrometer (Figure 2.4). The three pairs of wells were spaced 7.96 ± 0.07 mm, 5.95 ± 0.08 mm, and 3.93 ± 0.19 mm apart, as measured by micrometer from center to center of the wells. These wells were filled with 20-fold diluted Resovist particles (20 μ M iron, Bayer-Schering, Berlin, Germany), a commercially-manufactured SPIO tracer developed for MRI [5].

2.3.2 Berkeley X-Space Relaxometer

The Berkeley MPI relaxometer (Figure 2.2b,c) measures the x-space PSF without an imaging gradient [41, 57]. This system has an analogous goal as the MPI spectrometer, which is tailored to harmonic reconstruction methods [70, 71]. Unlike the spectrometer, this device measures information solely in the time domain, so it is suitable for the x-space reconstruction

method. The system has an electromagnetic drive coil and a bias coil. Varying the bias field enables us to simulate moving a point source sample in a gradient field. The virtual FFP is scanned using a resonant drive coil, and the signal is received by an inductive receiver coil.

The bias coil is driven by an audio amplifier (AE Techron LVC5050, Elkhart, IN, USA) at bias fields up to ± 180 mT. The drive coil generates a sinusoidal magnetic field of 10-200 mT-pp strength at frequencies ranging from 1.5 kHz to 11.5 kHz and is driven by an audio amplifier (AE Techron LVC5050, Elkhart, IN, USA). The signal is received using a gradiometric receive coil and is digitized by a 12-bit data acquisition system at 10 MSPS (National Instruments PCI-6115, Austin, TX, USA). Custom software written in MATLAB (Mathworks MATLAB, Natick, MA, USA) controls the system. We performed phase matching using an inductive pick-up coil and by further calibrating phase with a SPIO sample (50 nm hydrodynamic diameter fluidMAG nanoparticles by Chemicell, Berlin, Germany), which had negligible relaxation times. We measured the PSFs of Resovist particles (Bayer-Schering, Berlin, Germany) in the relaxometer.

Here the partial FOV method was employed, similar in goal to the focus-field methodology of Philips [72, 73, 74], but with some crucial distinctions in implementation, as detailed in [42, 44, 75]. Numerous overlapping partial FOVs are employed to cover a full FOV. The drive field strength determines the size of each partial FOV. A homogeneous DC field is progressively adjusted to offset the partial FOV center points, ensuring overlap between partial FOVs. This allows for reconstructing a much wider spatial FOV. During reconstruction these partial FOVs are stitched together to create the full PSF. Because we lose the first harmonic content of the MPI signal, we perform a DC recovery algorithm during this reconstruction [42, 43, 44].

2.3.3 Theoretical Calculations

Theoretical x-space signals were computed using MATLAB software (Mathworks MATLAB, Natick, MA, USA). The adiabatic x-space theoretical signal was calculated using Equation 2.2, and the non-adiabatic x-space theoretical signal was calculated using Equation 2.10 with an exponential decay term for the convolution kernel $r(t)$. A log normal distribution of SPIO diameters was used to calculate the H_{sat} and m variables in $s_{adiab}(t)$. The relaxation term $r(t)$ was calculated based on a relaxation time parameter, τ . Although the relaxation time could be calculated based on a theoretical prediction of τ , which often depends on the distribution of SPIO diameters, we used a single time constant, which we estimated by data fitting, as described in Section 2.3.4. The theoretical signal response for 10 cycles of the drive field was sampled at a rate corresponding to an analog sampling rate of 2 MHz, which is adequate to capture relaxation times approaching a microsecond. The drive field was chosen as a sinusoid with the frequency and field strength of the relaxometer (Section 2.3.2). Signal responses for the positive and negative scanning directions were separated based on whether the FFP velocity was positive or negative.

2.3.4 Fitting Algorithm for Relaxation Time Measurements

The experimental relaxometer signals were fit using a nonlinear least-squares optimization method that assumes a log normal particle size distribution and a single relaxation time

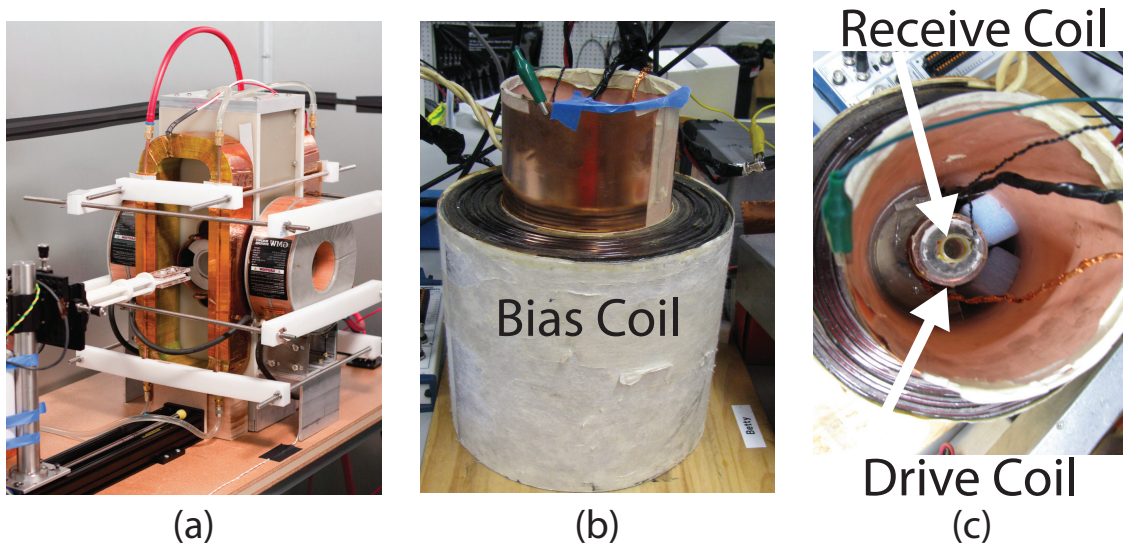


Figure 2.2: The Berkeley x-space projection MPI scanner (a) acquires two-dimensional images. A 2.3 T/m magnetic gradient creates a field-free-line (FFL), and the drive coil scans this FFL at 22.9 kHz with field strengths up to 35 mT-pp. The Berkeley x-space relaxometer, shown with side (b) and top (c) views, measures the point spread function of a particle sample. The drive coil generates a sinusoidal magnetic field of 10-200 mT-pp strength at frequencies of 1.5-11.5 kHz. The signal received from the gradiometric receive coil is digitized at 10 MSPS without filtering. The bias coil can add ± 180 mT field for partial field of view scanning.

constant. The fitting algorithm calculates theoretical signals, as described in Section 2.3.3, for each candidate particle size distribution and relaxation time. All fitting algorithms were performed using only the theoretical and experimental signals in the positive scanning direction. The experimental signal was acquired with a single FOV in the Berkeley x-space relaxometer. The best estimate of the nanoparticle relaxation time τ was solved by minimizing the error between the data and the theory. Good correspondence between this method's fitted SPIO diameter distribution and with size measurements using transmission electron microscopy was previously shown in [57].

2.4 Results

2.4.1 Relaxation Blurs the X-Space Image in the Scanning Direction

We calculated MPI point spread functions according to both the adiabatic and non-adiabatic x-space theories (Equations 2.2 & 2.10, respectively) for two experimental scenarios, one in the Berkeley x-space projection MPI scanner (Figure 2.3a,b) and the other in the Berkeley x-space relaxometer (Figure 2.3c,d). All theoretical PSFs were normalized with the adiabatic theoretical signal. Comparing the non-adiabatic signals to the adiabatic signals, relaxation in

the non-adiabatic x-space theory caused a loss in SNR of the signal and caused an asymmetric blur in the scanning direction of the image. This blur spatially shifts the peak signal in the image and increases the PSF’s full-width at half-maximum (FWHM), which we use to define our MPI resolution [76]. As these image effects were seen in the scanning direction, the reconstructed theoretical images for the positive and negative scanning directions were not identical.

2.4.2 MPI X-Space Theory with Relaxation Predicts Point Spread Function

2.4.2.1 Berkeley X-Space Projection MPI scanner

The calculated adiabatic and non-adiabatic x-space PSFs were compared with experimental PSF data obtained for Resovist particles in the projection MPI scanner. For the non-adiabatic theory, the (single) relaxation time constant was estimated from a single-FOV PSF of Resovist measured in the relaxometer under equivalent scanning conditions. These theoretical signals were compared to a one-dimensional profile through a scanner image of an amount of undiluted Resovist ($2 \mu L$), small enough to act as a point source (Figure 2.3a,b). Both the experiment and the theory are illustrated for the positive scanning direction only. Both theoretical signals were normalized with the adiabatic theoretical signal, and the experimental signal was normalized with the non-adiabatic theoretical signal for illustration purposes. The adiabatic x-space theory predicted the PSF to have a FWHM of 2.0 mm, whereas the non-adiabatic x-space theory predicted a FWHM of 3.1 mm. The experimental PSF of the scanner image had a FWHM measurement nearly identical to that of the non-adiabatic theory, 3.1 mm. Non-adiabatic calculations used a measured time constant of 2.9 μs . Scan time was 37 s and FOV was 6.6 cm x 5 cm.

2.4.2.2 Berkeley X-Space Relaxometer

We also calculated the adiabatic and non-adiabatic x-space theoretical PSFs using the same scanning parameters as a relaxometer measured PSF for Resovist particles (Figure 2.3c,d). To calculate the non-adiabatic theoretical PSF, we used a relaxation time constant (4.7 μs), which was measured under identical scanning conditions (see Section 2.3.4). Both theoretical PSFs were normalized with the adiabatic theoretical PSF. The experimental PSF was then normalized with the non-adiabatic theoretical PSF for illustration purposes. The adiabatic theoretical signal predicted the FWHM of the PSF to be 4.8 mT, whereas the non-adiabatic theory predicted a FWHM of 9.7 mT. The FWHM of the experimentally measured PSF was 10.7 mT.

2.4.3 MPI X-Space Theory with Relaxation Predicts Experimental Images

We scanned a line resolution phantom of 20-fold diluted Resovist in the Berkeley x-space projection MPI scanner and compared a one-dimensional profile through the center of the

acquired positive velocity image to the predictions of the adiabatic and non-adiabatic x-space theories (Figure 2.4). For the non-adiabatic x-space theory, we used the measured relaxation time (2.9 μ s) for Resovist in the Berkeley x-space relaxometer under equivalent scanning conditions (Section 2.3.4). We normalized the one-dimensional image profiles of both the theories to the experimental image profile. Scanning direction dependencies are demonstrated in the experimental profile as the right well in each well pair has a higher peak than the left well as some of the signal in the left well has been blurred to the right (the positive scanning direction). Additionally, the experimental profile is blurred much further in the positive scanning direction than the profile predicted by the adiabatic x-space theory, whereas the non-adiabatic theory shows similar widths as and excellent alignment with the experimental profile. Scan time of 59 s and a FOV of 13 cm x 5 cm, and no deconvolution was performed.

2.5 Discussion

The incorporation of Debye first-order relaxation modeling into the x-space analysis of MPI resulted in several predictions, including:

1. *Asymmetric, Increased Blurring:* Relaxation caused a temporal lag in SPIO response, which blurred the PSF in the scanning direction of the spatial domain after x-space reconstruction. Blurring due to relaxation caused a spatial shift in peak signal that alternates in the positive and negative directions. Relaxation also increases total blur, as measured by overall FWHM.
2. *SNR Loss:* Due to relaxation blurring, the peak MPI signal amplitude decreases since the rate of change of flux is slowed. Because the noise was unchanged, this decrease in signal becomes a loss in SNR.

Overall, the simple Debye first-order non-adiabatic x-space analysis showed excellent agreement with experimental data. The addition of relaxation effects improved agreement between the x-space theory and experimental images acquired from point sources and the more complex line resolution phantom in the Berkeley x-space projection MPI scanner. The adiabatic x-space theory consistently predicted superior spatial resolution than the obtained experimental data, whereas the non-adiabatic x-space theory consistently predicted spatial resolution consistent with the data. The non-adiabatic theoretical signal had a similar shape and FWHM compared to the experimental relaxometer signal, whereas the adiabatic theory did not accurately predict the complex shape and asymmetry of the experimental relaxometer signal. It is important to note that the measured relaxation times for the two MPI systems were quite different, resulting in different degrees of relaxation-induced blurring. We believe these differences in relaxation times are due to the differences in operating frequency of the two systems, which will be an important future subject of research in order to minimize relaxation-induced blurring.

This non-adiabatic description of x-space MPI accounts for the observed asymmetry between the positive and negative directions of scanning. Most noticeably, it explains an asymmetric blurring and associated shifting artifact which were always evident in experimental data. In a rectilinear trajectory in x-space in which every other line is scanned in

the opposite direction, in the resulting image, every other line would be shifted and blurred in the opposite direction. This even/odd artifact could be mitigated by using only positive (or negative) scanning direction data in a two-dimensional image reconstruction. Another alternative could be to use both even and odd scanning directions and a phase recovery algorithm to create a symmetric impulse response. Despite this blurring in the scanning direction, x-space reconstruction still produces an image, albeit with a moderate loss in resolution.

This work represents the first experimental and theoretical exploration of the effects of relaxation, which has been neglected in both system matrix reconstruction and x-space reconstruction. This enhanced knowledge of how relaxation impacts the image can enable us to minimize these negative effects. SPIO characteristics can be tailored for excellent MPI resolution by maximizing the magnetic capabilities while minimizing relaxation parameters [8, 67]. We can also explore how MPI scanning parameters affect relaxation effects so that MPI scanning sequences can be designed for optimal resolution for a given SPIO. Relaxation blurring may also be reduced with post-processing methods. By experimentally measuring the relaxation process *in vivo*, one could deconvolve the effects of relaxation using well known methods of image processing. Deconvolution would of course increase noise [77], implying that an optimal tradeoff could be explored. Understanding relaxation and its consequences will help us to improve MPI image quality.

The current work relies on only a single relaxation time constant, yet it seems to adequately predict experimental data. Clearly, more sophisticated relaxation models, similar to the thorough work in [61] may offer improvements. Multiple relaxation times or multiple relaxation mechanisms should certainly be explored as they may be present in the *in vivo* environment.

This direction of research holds exciting potential for future molecular and cellular imaging applications of MPI. Relaxation times may be used to monitor *in vivo* parameters, in combination with SPIOs labeled with ligands designed to alter their dominant relaxation mechanism. For example, one could imagine using MPI to monitor *in vivo* viscosity [65], perhaps with no ligand. MPI may also be used one day to visualize protein or cell binding via relaxation measurements of a SPIO labeled with a tailored ligand [78, 79]. Of course, these emerging MPI molecular and cellular imaging methods must be explored with both x-space and harmonic reconstruction schemes.

2.6 Conclusions

The non-adiabatic x-space theory is the first example of a MPI system theory and reconstruction scheme that accounts for relaxation effects. The non-adiabatic x-space theory showed excellent agreement with experimentally measured signals from both the Berkeley x-space relaxometer and the Berkeley x-space projection MPI scanner. Our data indicates that relaxation modeling is crucial to modeling the MPI signal. Relaxation caused a loss in SNR and an asymmetric blurring of the image in the scanning direction. We demonstrated that a simple modification to x-space reconstruction produces robust image reconstruction. Understanding relaxation's effect on the image will help researchers to mitigate relaxation blurring and to design SPIOs and x-space scanning methods for optimal image quality.

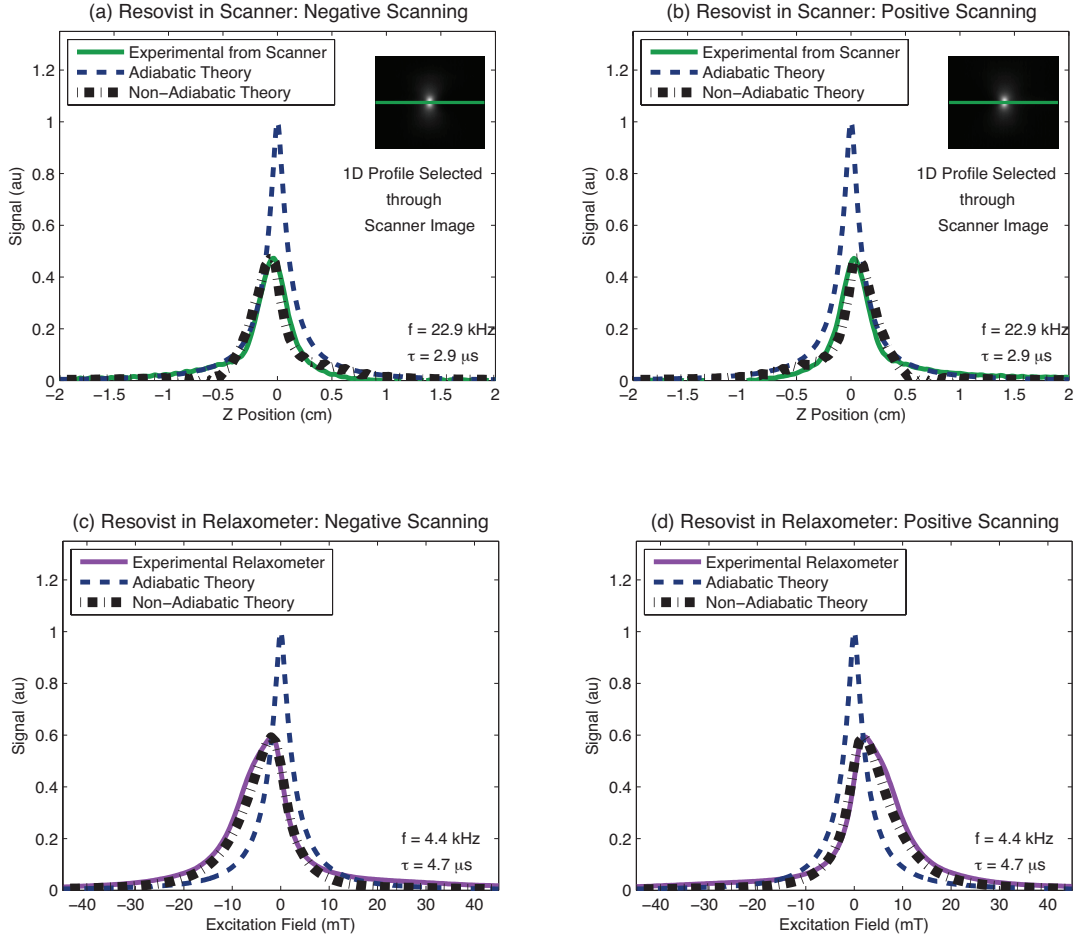


Figure 2.3: Experimentally-measured PSFs displayed alongside theoretical PSFs calculated from the adiabatic and the non-adiabatic x-space theory for each scanning direction. The inclusion of relaxation into the theory predicted a significant loss in predicted resolution and peak signal and produced a shape which more closely resembled that of the experimental signal. (a,b) We compared the x-space theoretical PSFs to a one-dimensional profile through (inset) a positive-velocity scan image of $2 \mu L$ of undiluted Resovist acquired in the projection MPI scanner with a drive field of 20 mT-pp at 22.9 kHz. (c,d) We measured a PSF of Resovist in the relaxometer with a drive field of 60 mT-pp at 4.4 kHz. ©2012 IEEE

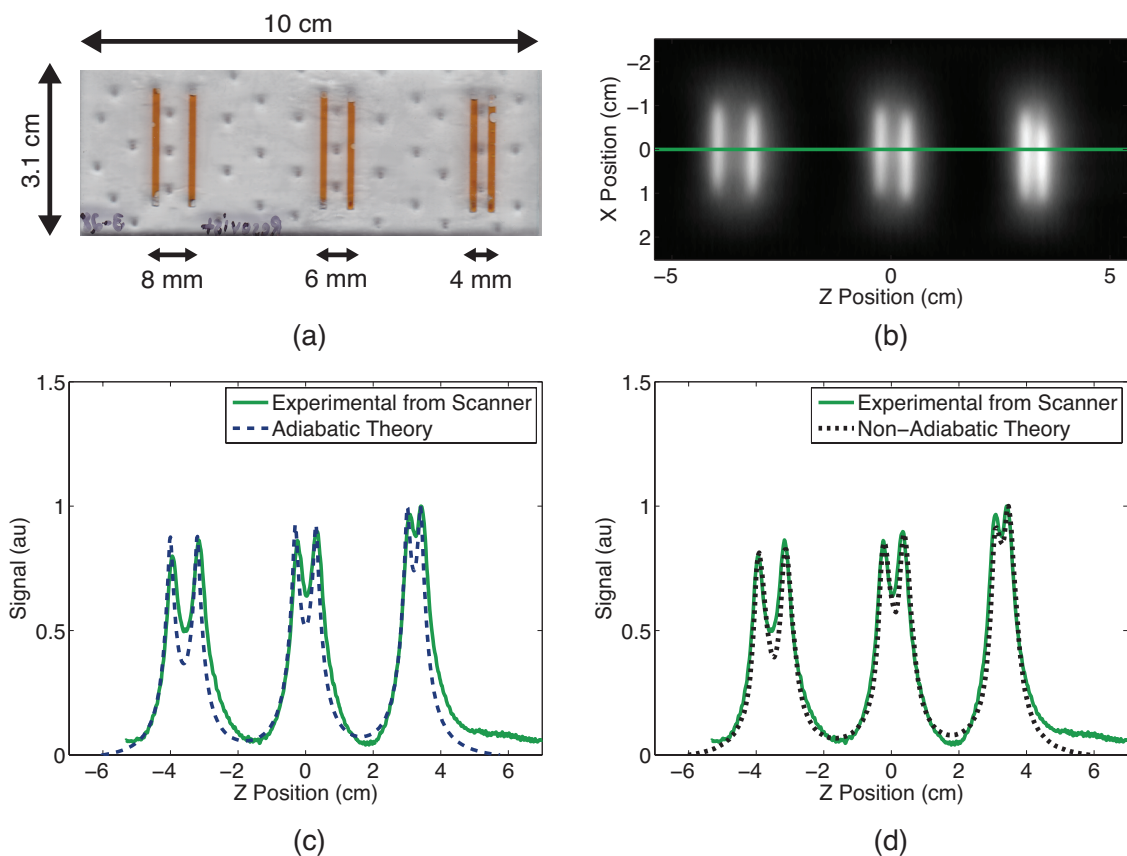


Figure 2.4: (a) A line resolution phantom was constructed with 1.75 mm wide wells which were filled with 20x diluted Resovist. We acquired (b) a positive-velocity scan image of this phantom in the projection MPI scanner at 20 mT-pp. We visualized a one-dimensional profile through the center of this image and compared this profile to the image predicted by (c) the adiabatic x-space theory and by (d) the non-adiabatic x-space theory. The experimentally-measured image showed better agreement with the non-adiabatic x-space theory than with the adiabatic x-space theory. ©2012 IEEE

Chapter 3

Effects of Drive Field on Relaxation-Induced Blurring in Magnetic Particle Imaging

Magnetic particle imaging (MPI) is a new imaging technology that acquires quantitative images of superparamagnetic iron oxide nanoparticles (SPIOs) with potential medical applications in angiography, cell tracking, and cancer detection. MPI promises excellent contrast, no depth penetration limitations, and high sensitivity. MPI detects the SPIO magnetization response to a sinusoidal excitation field, called a drive field. A phenomenon referred to as relaxation can delay the SPIO response, leading to image blurring and signal-to-noise ratio (SNR) loss. To study how the drive field influences relaxation, we measure spatial resolution and relative signal levels on a relaxometer and on a 3D MPI scanner at varying drive fields. We measure relaxation times in the relaxometer to study their drive field-dependence, and theoretically predict relaxation-induced blurring as a function of relaxation time and drive field parameters. We find that relaxation in MPI can be approximated as a frequency-independent phase lag and that the spatial resolution varies primarily with drive field amplitude. Specifically, we showed that spatial resolution improves at lower drive field amplitude, despite the fact that relaxation times are actually longer for these conditions. To balance resolution and SNR priorities, the optimal drive field may be a low field amplitude applied at a high frequency. Understanding how the MPI drive field affects relaxation and its adverse effects will aid in designing scanning sequences to minimize or exploit relaxation-induced blurring.

3.1 Introduction

In this work, we aim to investigate how MPI drive field parameters, namely the frequency and amplitude, impact relaxation times and subsequent relaxation-induced image blurring. We experimentally demonstrate that relaxation time constant decreases with faster scanning parameters, i.e., increasing drive field amplitude and/or frequency. In contrast, image blur is minimized by decreasing the drive field amplitude, with minimal changes due to drive field frequency. We determine that relaxation in MPI can be approximated as a frequency-

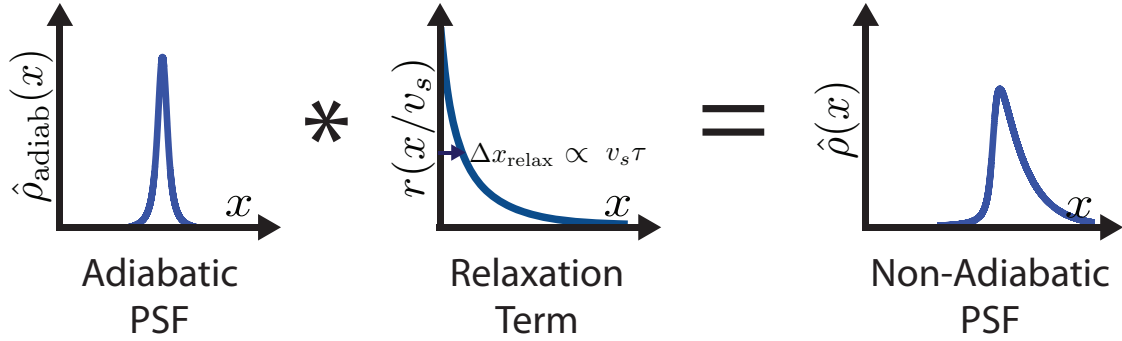


Figure 3.1: The adiabatic point spread function (PSF) is spatially convolved with a relaxation term $r\left(\frac{x}{v_s}\right)$, which blurs the image in the scanning direction. Relaxation-induced blurring, Δx_{relax} , increases with increasing relaxation time τ and with increasing drive field scanning rate v_s via either frequency or amplitude.

independent phase lag, and we use the non-adiabatic x-space theory for MPI to predict spatial resolution based on measured phase lags, the results of which compare well to the resolution measured on a MPI scanner. This knowledge will aid in selecting the optimal drive field frequency and amplitude range for MPI scanners, and will be essential in designing scanning sequences to minimize deleterious effects of relaxation or to exaggerate regions of differing relaxation properties.

3.2 Theory

First, we review the non-adiabatic x-space theory for MPI [80], which extended x-space MPI theory to include relaxation effects. We then describe a linear approximation of the sinusoidal MPI drive field. Last, we describe relaxation in the spatial domain, which highlights the drive field-dependency of relaxation-induced blurring for a given relaxation time.

3.2.1 Review of Non-Adiabatic X-Space Theory for MPI

The x-space theory for MPI was originally derived assuming negligible relaxation effects [41]. In Section 2.2.2, we modeled relaxation using a Debye process [46, 52]. This model showed that nanoparticle relaxation blurs the adiabatic x-space signal, $s_{\text{adiab}}(t)$, with a relaxation term $r(t)$. The resulting MPI signal equation is:

$$s(t) = s_{\text{adiab}}(t) * r(t) \quad (3.1)$$

$$= \gamma \left(\dot{x}_s(t) \rho(x) * \dot{\mathcal{L}} \left[\frac{Gx}{H_{\text{sat}}} \right] \Big|_{x=x_s(t)} \right) * r(t) \quad (3.2)$$

where

$$h(x) = \dot{\mathcal{L}} [Gx/H_{\text{sat}}] \quad (3.3)$$

Here, $\gamma = \frac{B_1 m G}{H_{sat}}$ is a scalar term, B_1 [T/A] is the sensitivity of the receive coil, m [A·m²] is the magnetic dipole moment, G [T/m/ μ_0] is the magnetic field gradient, H_{sat} [T/ μ_0] represents how much field is required to saturate the SPIO sample, $x_s(t)$ [m] is the instantaneous FFP position, $\dot{x}_s(t)$ [m/s] is the FFP velocity, $\rho(x)$ [nanoparticles/m] is the 1D SPIO density, and $h(x)$ is the point spread function (PSF). The PSF is the derivative of the Langevin function of paramagnetism [41, 40], $\mathcal{L}[\bullet]$. Note that the first convolution operation inside the parenthesis is a *spatial* convolution, and the second is a *temporal* convolution.

The non-adiabatic x-space imaging equation was also derived in Section 2.2.2, and we demonstrated that it is well approximated by a temporal convolution of the adiabatic image $\hat{\rho}_{adiab}(x_s(t))$ with the relaxation kernel $r(t)$:

$$\hat{\rho}(x_s(t)) \approx \hat{\rho}_{adiab}(x_s(t)) * r(t) \quad (3.4)$$

$$\approx \left(\rho(x) * h(x)|_{x=x_s(t)} \right) * r(t) \quad (3.5)$$

Again, the SPIO density is *spatially* convolved with the adiabatic PSF and *temporally* convolved with the relaxation term.

We need to translate this temporal convolution to *space* assuming a linear approximation for the drive field and that $r(t)$ is a Debye (exponential) process. In this work, we will focus on experimentally investigating blur from the relaxation kernel, $r(t)$, under varying drive field frequency and amplitude.

3.2.2 Linear Approximation for Sinusoidal Drive Fields

MPI scans the FFP using a sinusoidal drive field, $H(t) = H_{amp} \sin(2\pi f_0 t)$, which is approximately linear about $H(t) = 0$. If we perform a first-order Taylor expansion, we arrive at a linear approximation for the drive field:

$$H(t) \approx 2\pi f_0 H_{amp} t \quad (3.6)$$

where H_{amp} [T/ μ_0] is the peak amplitude and f_0 [Hz] is the frequency of the drive field. The derivative of this equation is the magnetic field slew rate Gv_s [T/s/ μ_0] [41]:

$$Gv_s = 2\pi f_0 H_{amp} \quad (3.7)$$

Dividing by the gradient strength G , we arrive at the scanning rate v_s [m/s]:

$$v_s = \frac{2\pi f_0 H_{amp}}{G} \quad (3.8)$$

3.2.3 Relaxation in the Spatial Domain

To convert the time integral in Equation 3.4 to an integral in space, we assume that the FFP is scanned linearly across the FOV with constant scanning rate, v_s , as given in Equation 3.8. This approximation is only valid when the drive field amplitude is near zero. We then

calculate the instantaneous FFP position as $x_s(t) = v_s t$ [m], and rewrite the non-adiabatic imaging equation (Equation 3.4) as:

$$\hat{\rho}(x_s(t)) \approx \hat{\rho}_{\text{adiab}}(x_s(t)) * \frac{1}{v_s} r\left(\frac{x_s(t)}{v_s}\right) \quad (3.9)$$

Here, assuming a linearly-varying drive field allows us to express the *temporal* convolution of Equation 3.4 as a *spatial* convolution with a relaxation kernel, $r(x_s(t)/v_s)$, that is a function of space, x , and scanning rate, v_s . Equation 3.9 thus shows the link between temporal blurring and spatial blurring (see Figure 3.1).

From Section 2.2.2, we use an exponential relaxation term derived from a first-order Debye process [46, 52, 80]:

$$r(t) = \frac{1}{\tau} \exp\left[-\frac{t}{\tau}\right] u(t) \quad (3.10)$$

where $u(t)$ is the Heaviside function and τ [s] is the relaxation time constant, which our experimental findings suggest is a function of drive field amplitude and frequency, i.e.,

$$\tau = \tau(H_{\text{amp}}, f_0) \quad (3.11)$$

Rewriting Equation 3.10 in the spatial domain we obtain:

$$r\left(\frac{x_s(t)}{v_s}\right) = \frac{1}{v_s \tau} \exp\left[-\frac{x_s(t)}{v_s \tau}\right] u(x_s(t)) \quad (3.12)$$

Ultimately we would like to understand how to optimize spatial resolution, and in particular, how to minimize relaxation-induced blurring. Here we describe resolution using the Full Width at Half Maximum (FWHM) definition, allowing straightforward comparison of the relative contributions to image blurring of two distributions with very different parameters, such as the Langevin function and the exponential relaxation kernel. We estimate the FWHM value of Equation 3.12 as:

$$\Delta x_{\text{relax}} = \ln(2) v_s \tau \quad (3.13)$$

This relation shows that relaxation-induced blur increases with increasing drive field amplitude, frequency, and relaxation time. If we translate this blurring process to the spatial frequency domain, we see relaxation is effectively a low-pass filter whose cut-off frequency is dependent on drive field amplitude, frequency, and relaxation time (See Section 3.7).

We can also write $r(x_s(t)/v_s)$ as a function of phase lag, ϕ [rad]:

$$r\left(\frac{x_s(t)}{v_s}\right) = \frac{G}{\phi H_{\text{amp}}} \exp\left[-\frac{G x_s(t)}{\phi H_{\text{amp}}}\right] u(x_s(t)) \quad (3.14)$$

where

$$\phi = 2\pi f_0 \tau \quad (3.15)$$

Here, phase lag expresses in radians the angle between the net magnetization vector and the applied drive field. Phase lag will be used in Section 3.4 to compare measured relaxation

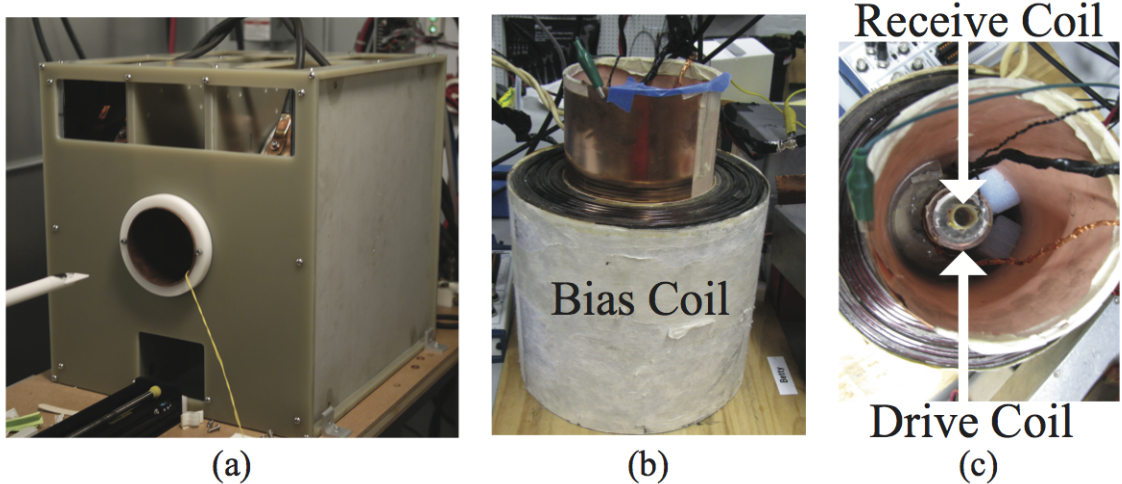


Figure 3.2: (a) The Berkeley 3D MPI scanner acquires three-dimensional images using a 7 T/m selection field. A drive coil scans the FFP of the scanner at 23.2 kHz at peak amplitudes up to 30 mT. The Berkeley relaxometer, shown with (b) side and (c) top views, measures the point spread functions (PSF) of SPIO nanoparticles. A sinusoidal magnetic field is generated in the drive coil at frequencies of 1.5-25 kHz and of 5-100 mT drive field peak amplitude. The MPI signal is acquired in a gradiometer receive coil through induction at 10 MSPS without filtering. The bias coil produces up to a ± 180 mT field.

times at different frequencies, and our experimental findings indicate that ϕ is approximately frequency-independent. We estimate Δx_{relax} in this form as:

$$\Delta x_{\text{relax}} = \frac{\ln(2) H_{\text{amp}} \phi}{G} \quad (3.16)$$

These equations describe how the relaxation term $r(x_s(t)/v_s)$ blurs the image according to the phase lag and the drive field amplitude (ϕH_{amp}). To translate this term from units of magnetic field [T/ μ_0] to units of space [m], ϕH_{amp} is divided by the magnetic field gradient G .

In this section, we derived the non-adiabatic image equation for a nanoparticle given an adiabatic PSF and a relaxation kernel. In the next sections, we use this mathematical approach to investigate relaxation on experimental imaging and non-imaging MPI systems, and we show how spatial resolution changes with drive field amplitude and frequency.

3.3 Methods

3.3.1 Berkeley 3D MPI Scanner

The MPI scanner (Figure 3.2a) used in this study acquires three-dimensional images with a drive coil that scans the FFP in the z direction (down the bore of the scanner) at 23.2 kHz

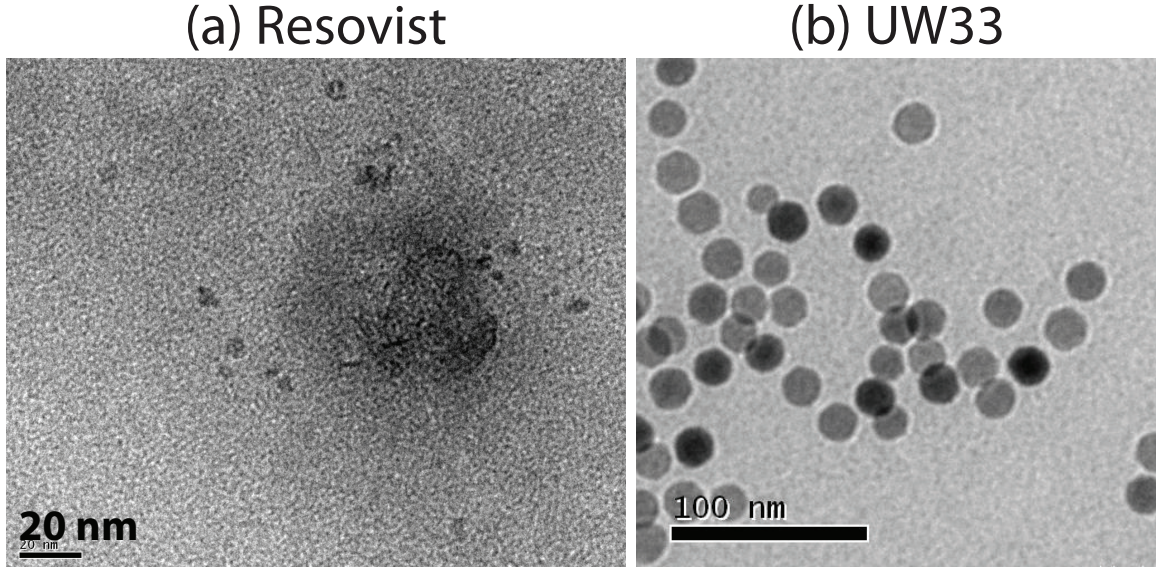


Figure 3.3: Transmission electron microscopy (TEM) images of two SPIO nanoparticle tracers: (a) Resovist (Bayer-Schering, Berlin, Germany), and (b) UW33, which was synthesized at the University of Washington.

at peak amplitudes up to 30 mT. The frequency of the MPI scanner is fixed, so only the drive field amplitude was varied to examine the effects of scanning rate on relaxation-induced blurring. The minimum drive field amplitude was selected as the lowest drive field amplitude with sufficient SNR. The magnetic field gradient is 7 T/m in the x-axis, and 3.5 T/m in the y- and z-axes. This system has been previously discussed in [29, 43].

We characterized the spatial resolution of Resovist particles in the scanner by imaging a “point source” phantom of 2 μ L undiluted Resovist (Bayer-Schering) shown in Fig. 3.5d. Here we use the Houston resolution criteria and express spatial resolution as FWHM [mm] [76], which we measured from a one-dimensional profile in the z direction (Figure 3.5b,c). Relaxation effects blur the image in the scanning direction, producing different images for the positive-velocity scan and the negative-velocity scan [80]. The spatial resolution measurements, then, are for an average of the resolutions (FWHM) of the positive- and negative-velocity scans. The phantom measured 1.0 mm in the z direction and 0.9 mm in the x direction. Scan time was 2 minutes 52 seconds for a 2 cm x 2 cm x 4.8 cm FOV.

3.3.2 Berkeley Relaxometer

As described previously in Section 2.3.2, the Berkeley relaxometer (Figure 3.2b,c) measures a SPIO sample’s PSF from which we can measure relaxation time, signal strength, and spatial resolution. Unlike an MPI scanner, it does not use a selection field. The relaxometer is similar in goal to a MPI spectrometer [70, 71], but it does not take the Fourier transform of the data since x-space theory does not need to measure harmonics for reconstruction [1, 40, 70, 71]. For this work, the drive field frequency range was extended to 1.5-25 kHz for drive field peak amplitudes of 5-100 mT. Again, drive field amplitudes lower than this range

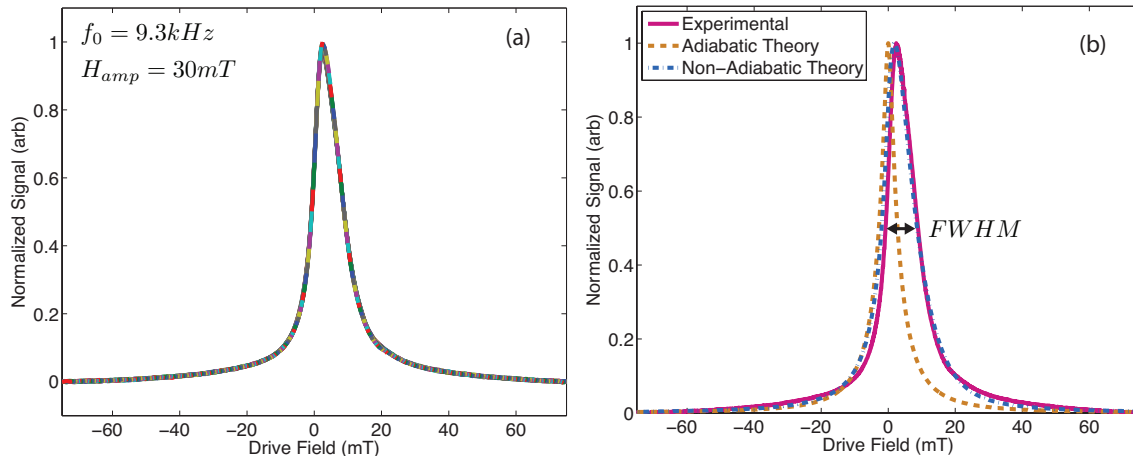


Figure 3.4: Example of a point spread function (PSF) of Resovist measured in the relaxometer using the partial field-of-view (FOV) method at a drive field of 30 mT peak amplitude at 9.3 kHz. Multiple partial FOVs were scanned while the bias coil applied a linear ramp from -75 mT to +75 mT. The partial FOVs, each shown as a different color in (a), were merged to form the unstitched PSF. Next, the partial FOVs were averaged to form (b) the stitched PSF, which compares well to the non-adiabatic theoretical PSF (calculated with a $2.3 \mu\text{s}$ relaxation time). The adiabatic theory predicts a more symmetric PSF with less blur, which does not capture the effects of relaxation.

were limited due to SNR.

We measured two samples in the relaxometer: undiluted Resovist particles (0.5 mM Fe, Bayer-Schering, Berlin, Germany), a commercially-manufactured SPIO tracer originally developed for MRI [5], and UW33, a sample synthesized at the University of Washington [8, 9]. Images acquired by transmission electron microscopy (TEM) (FEI Tecnai 12) show that the University of Washington particles contain a single iron oxide core (Figure 3.3b), whereas Resovist particles are believed to contain *clusters* of small iron oxide cores immobilized in a carboxydextran composite (Figure 3.3a) [81, 82].

For relaxometer experiments, the peak signal was measured as the maximum value of the filtered signal in the time domain. Spatial resolution and relaxation time were measured from the PSFs reconstructed using the partial FOV method. Peak signal, spatial resolution, and relaxation time were all measured from the same data. A detailed explanation of these measurements is described below.

3.3.3 Partial FOV Scanning to Measure Spatial Resolution

For all the relaxometer data in this work, we used the bias coil (Figure 3.2b) to employ the partial FOV method, also called the focus field method, to acquire a PSF across a larger range of fields. As described in Section 2.3.2, we can acquire multiple partial FOVs that are stitched together to compose a large total FOV (Figure 3.4) [42, 43, 44]. The smaller FOVs that are stitched into a full FOV can also be called imaging stations [72, 73, 74].

The bias coil applied a linear ramp from -75 mT to +75 mT, which was applied simul-

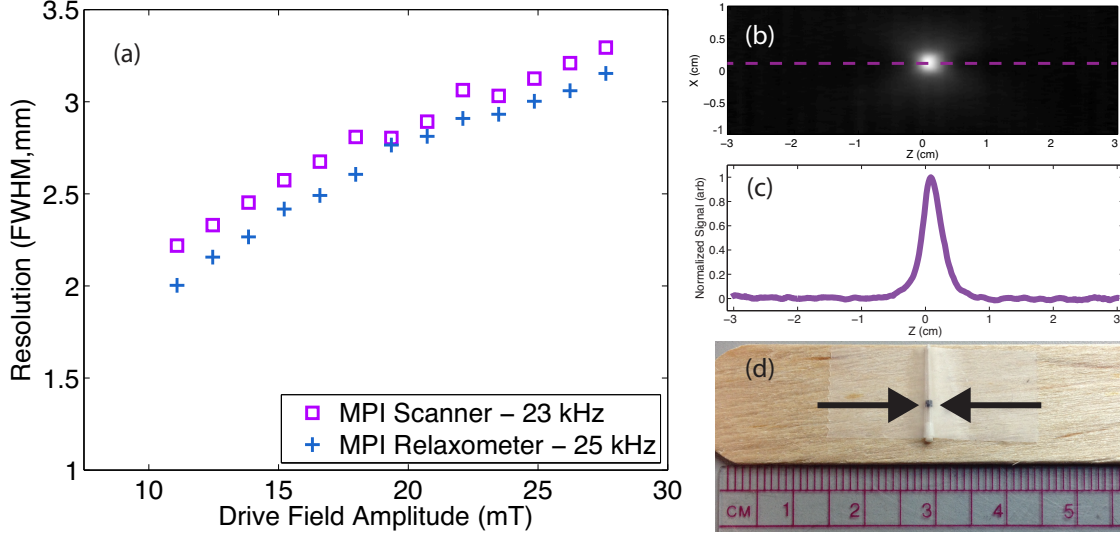


Figure 3.5: (a) Spatial resolution of (d) a point source of undiluted Resovist nanoparticles ($2 \mu\text{L}$) deteriorated as the 3D MPI scanner drive field amplitude increased and was comparable to resolution measured in the relaxometer at a similar frequency (23.2 kHz for the MPI scanner vs. 25 kHz for the relaxometer). Resolution was measured as the full-width at half maximum (FWHM) width of (c) the 1D profile in the z direction through the center of (b) the image in the xz -plane. The reported value is the average of the negative- and positive-velocity scan images. Here, only the positive-velocity image is displayed. Scan time was 2 minutes 52 seconds for a FOV of 2 cm x 2 cm x 4.8 cm. Relaxometer-measured resolution was converted to units of space using the same magnetic field gradient (3.5 T/m in the z direction) as the MPI scanner.

taneously with the drive field. We acquired one thousand partial FOVs while covering the total FOV of 150 mT-pp (peak-to-peak). Since the linear approximation of the drive field is only valid about the zero-crossings of the drive field (see Section 3.2.2), only the center 20% of each partial FOV was used in the computation of the PSF. Again, we use the Houston resolution criteria and measure spatial resolution as the FWHM [mT] width of the PSF [76]. To convert resolution measured in the relaxometer in units of applied magnetic field [mT] to units of length [mm], we divided the measured FWHM value by the magnetic field gradient of the MPI scanner (3.5 T/m in the z direction).

Prediction of the non-adiabatic spatial resolution (FWHM) Δx [m] of the MPI image given an adiabatic PSF and a relaxation kernel is problematic, since there is no closed form solution for the convolution of the adiabatic PSF (approximately a Lorentzian) and the relaxation kernel (an exponential) given in Equation 3.9. We have found that we can reasonably approximate the non-adiabatic FWHM as a weighted sum of the adiabatic resolution Δx_{adiab} [m] and the blur from relaxation Δx_{relax} [m], i.e.,

$$\Delta x \approx \alpha \Delta x_{\text{adiab}} + \beta \Delta x_{\text{relax}} \quad (3.17)$$

We estimated the weightings α and β through a non-linear least-squares regression to the true

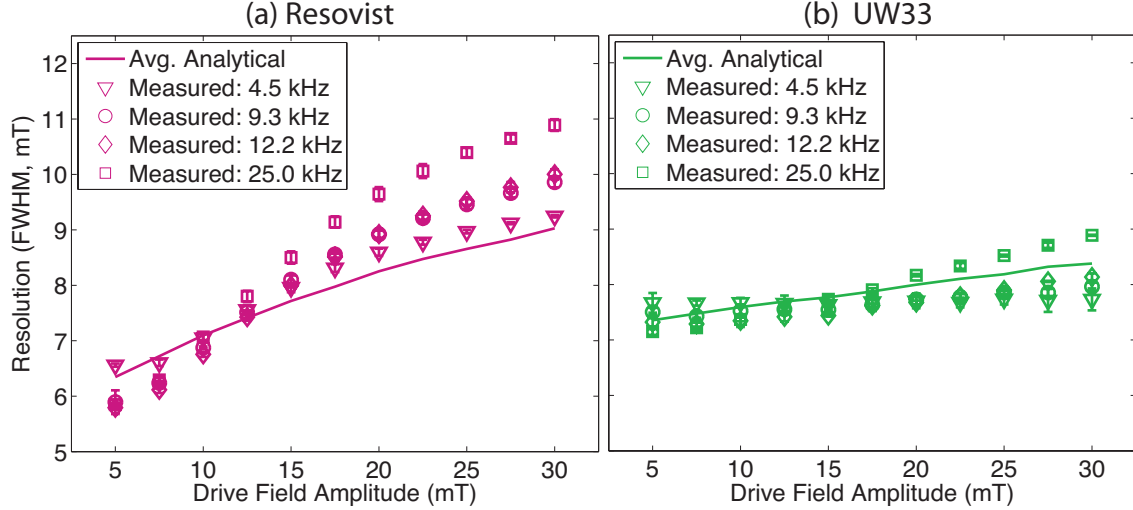


Figure 3.6: Relaxometer-measured resolution for (a) Resovist and (b) UW33 deteriorated with increasing drive field amplitude, and showed relatively modest changes with frequency. Resovist experiences more resolution deterioration than UW33 with increasing drive field amplitude. Theoretical predictions of resolution (solid lines) calculated from average phase lags showed comparable values to measured resolution (shapes). Resolution was measured as the full-width at half maximum (FWHM) widths of point spread functions (PSFs) acquired in the relaxometer using partial field-of-view methods. Error bars indicate the standard deviation from the average value for three sets of data.

resolution (FWHM) calculated from the non-adiabatic x -space image relation in Equation 3.9. For a realistic range of SPIO sizes (15-23 nm diameter) and $v_s\tau$ between 0.2-10 mT, the weightings that provide the best fit were $\alpha = 0.96$ and $\beta = 1.38$. Note that these optimal weightings are independent of the selection field strength, G , as it is a common denominator for Δx_{adiab} and Δx_{relax} . We computed theoretical resolutions (FWHM) according to Equations 3.16 and 3.17 using the aforementioned SPIO sizes for Resovist and UW33, as well as the average phase lag measured at each drive field amplitude.

3.3.4 Fitting Algorithm to Measure Relaxation Times

A fitting algorithm was used to estimate the relaxation times from PSFs measured in the relaxometer. Theoretical PSFs were calculated using Equation 3.4 with the relaxation term $r(t)$ defined in Equation 3.10 for a large range of candidate relaxation times. Each PSF was calculated for a single relaxation time and a log-normal SPIO magnetic core diameter distribution. For Resovist, we used 17 ± 4 nm for the magnetic core diameter distribution (mean \pm standard deviation). For UW33, we used 20 ± 2 nm for the magnetic core diameter distribution measured using a TEM and ImageJ software (National Institutes of Health). Magnetic core diameters were chosen based on previous studies [42, 44, 57, 83].

We estimated the relaxation time of an experimental PSF as the τ that minimized the weighted least-squares error between the theoretical and experimental PSF. Note that the theoretical PSFs were calculated using the same acquisition parameters, such as drive field

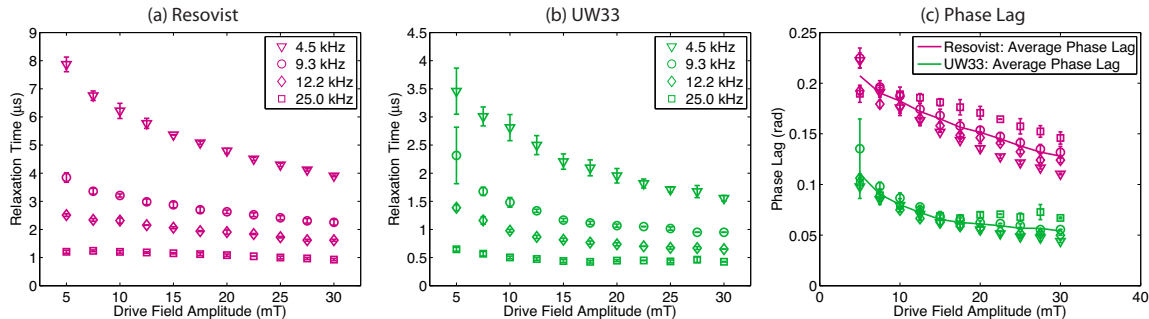


Figure 3.7: Relaxation times of (a) Resovist and (b) UW33 measured in the relaxometer decreased with increasing magnetic slew rate, which was varied by increasing both drive field amplitude (5-30 mT) and frequency (4.5, 9.3, 12.2, and 25 kHz). While relaxation times showed greater decreases with field amplitude at the lower frequencies, (c) phase lags were comparable across the tested range of frequencies. Measured relaxation times were translated to phase lags by multiplying by 2π and the drive field frequency. The phase lags averaged across the four frequencies are displayed as the solid lines in (c).

amplitude and frequency, as the experimental data. All computations were performed in MATLAB (Mathworks MATLAB, Natick, MA, USA).

3.4 Results

Resolution (FWHM) of Resovist in the MPI scanner deteriorated with increasing drive field amplitude and corresponded well to those acquired in the relaxometer at a similar frequency (Figure 3.5a). For relaxometer experiments, resolution (FWHM) of Resovist consistently deteriorated with increasing drive field amplitude at four different drive field frequencies (4.5, 9.3, 12.2, and 25 kHz) (Figure 3.6a). Similarly, resolution (FWHM) of UW33 also deteriorated with increasing drive field amplitude (Figure 3.6b); however the changes in UW33 resolution (FWHM) were relatively small ($<15\%$) compared to that of Resovist with drive field amplitude ($>40\%$). For both samples, resolution (FWHM) showed modest changes with drive field frequency, with the most noticeable difference occurring between 12.2 and 25 kHz (Figure 3.6a,b).

Measured relaxation times of Resovist and UW33 decreased with increasing drive field amplitude and frequency, as shown for four frequencies, 4.5, 9.3, 12.2, and 25 kHz, in Figures 3.7a-b. While the UW33 sample showed similar behavior in response to varying magnetic slew rate parameters as Resovist, its measured relaxation times were approximately half that of Resovist at each measured magnetic slew rate.

In Figure 3.7c, we calculate phase lags from the measured relaxation times using Equation 3.15. The average phase lag across the four frequencies is also calculated for each sample and displayed as the solid lines in Figure 3.7c. When we compare Figures 3.7a,b and 3.7c, we can see that although the relaxation times decrease with increasing frequency, they remain somewhat constant when viewed as phase lags. This phenomenon helps explain why resolution (FWHM) shown in Figure 3.6 showed only modest changes with drive field frequency.

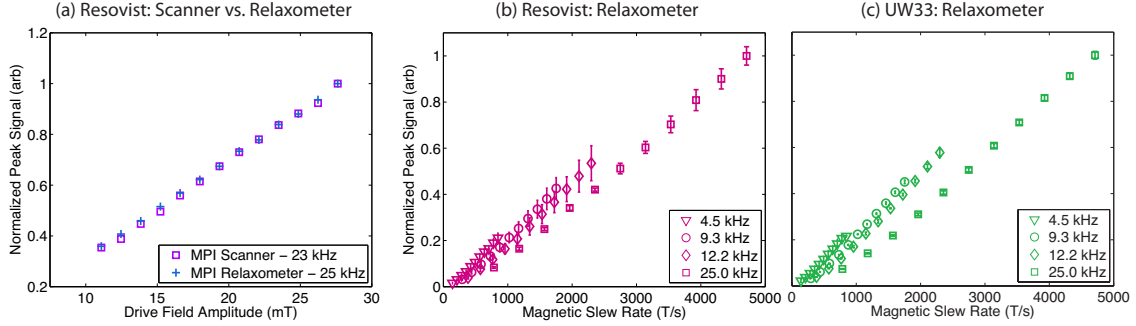


Figure 3.8: (a) Peak signal increased linearly with drive field amplitude for point sources of Resovist measured in the 3D MPI scanner and in the relaxometer at 23 kHz and 25 kHz, respectively. These values were normalized to the peak signal of the 27.6 mT data for comparison. Peak signal increased linearly with magnetic slew rate, increased via drive field amplitude and frequency, for (b) Resovist and (c) UW33 measured in the relaxometer at 4 frequencies (4.5, 9.3, 12.2, and 25 kHz) at a range of 5-30 mT amplitude. The peak signals in (b) and (c) were normalized to the peak signal acquired at the highest magnetic slew rate, 4710 T/s.

We calculated the theoretical resolution from Equations 3.17 and 3.16, using the average phase lags from Figure 3.7c (shown with solid lines). The resulting theoretical resolution (FWHM) deteriorated with increasing drive field amplitude (shown with solid lines Figure 3.6), and compared well to the measured values of resolution.

Peak signal increased linearly with increasing drive field amplitude for Resovist in both the MPI scanner and the relaxometer (Figure 3.8a). Similarly, peak signal increased linearly with increasing drive field magnetic slew rate for both Resovist and UW33 in the relaxometer (Figures 3.8b,c). When compared across frequencies, peak signal increased approximately linearly with increasing slew rate, independent of the specific drive field frequency or amplitude. Peak signal data in Figure 3.8a were normalized to that acquired at the highest drive field amplitude, and peak signal data in Figure 3.8b-c were normalized to that acquired at the highest magnetic slew rate.

3.5 Discussion

Adiabatic MPI theory was derived assuming instantaneous response of the magnetic nanoparticles to the applied field [40, 41, 42]. Unfortunately, adiabatic theory does not accurately model real-world behavior, and so we extended this theory to better model the measured nanoparticle responses. We demonstrated previously that this extended model is more accurate [80], but our previous work did not investigate how scanning parameters may affect relaxation times and subsequent relaxation-induced blurring. *We see that the primary factor that affects MPI resolution for Resovist and UW33 is the drive field amplitude (Figure 3.6), and not the drive field frequency.* We must emphasize that this result may not be the case for other nanoparticles.

The worsening of resolution occurs despite determining that relaxation times *decrease*

with greater drive field amplitude (Figure 3.7). This reduction of relaxation time is consistent with the findings of other works [49, 57]. In addition, we observed that relaxation time constants decrease when scanning with faster drive field slew rates, both for increasing amplitudes *and* frequencies.

The link between relaxation time and resolution can be quite complex, as both the relaxation times and the process of translating them to a spatial blur are dependent on drive field amplitude and frequency. We find that it is descriptive to express relaxation as a phase lag, similar to prior work [54]. Our results showed that the drive field *amplitude* is the strongest driver of phase lag, while drive field *frequency* has a much less pronounced effect. Although relaxation times decrease at higher frequency, the shorter relaxation times are still significant compared to the shorter period of the higher frequency scan. Phase lag may be a better descriptor for MPI relaxation than the relaxation time constant, τ , as it is an approximately frequency-independent indicator of how the SPIO magnetic moment lags behind the drive field.

Next, we derived that relaxation blur (Δx_{relax}) is a function of phase lag and drive field amplitude (ϕH_{amp}). Although stronger drive field amplitudes reduce SPIO phase lag, relaxation-induced blurring *deteriorates* with increased drive field amplitude. As seen in Equation 3.14, the spatial image domain, x , is blurred by the term ϕH_{amp} , which can be converted to spatial units by dividing by the magnetic field gradient G . Similar to the relationship between relaxation time constant and frequency, *decreased* phase lags at higher drive field amplitude can translate to *increased* spatial blur after weighting phase lags by drive field amplitude. These predicted trends were also seen in the experimentally-measured resolution data.

The changes in phase lag of Resovist with respect to drive field amplitude were larger than those of UW33, translating into larger resolution changes. In our investigations of many SPIO samples, we find that SPIO relaxation behavior seems to fall into one of two categories: single-core particles with minimal aggregation tend to show minimal resolution change with drive field parameters (like UW33), while multi-core particles show resolution improvement with decreasing drive field amplitude (similar to the trend of Resovist). Particles such as UW33, which maintain low phase lags even at high drive field amplitudes, may enable higher SNR while preserving resolution. It is possible that these two different families of particles relax via different physical mechanisms.

Tailoring SPIOs for MPI and careful control of the magnetic properties including the relaxation mechanism is an emerging field of research for improving MPI sensitivity and resolution [8, 9, 67]. Magnetic core size, anisotropic characteristics, and polymer coating characteristics may all play a role in a nanoparticle’s relaxation from physical rotation, akin to Brownian relaxation, or magnetic reversals within the iron oxide, or Néel relaxation. Exploring the various types of relaxation mechanisms, and tailoring particle design to MPI, will be an important area of research for both SPIO optimization and blur-minimizing MPI sequence design.

Unlike resolution, SNR improves with increasing scanning rate [41]. We observed a linear gain in peak signal with increasing magnetic slew rate, via increasing drive field frequency or amplitude. Therefore, there will be a trade-off between resolution and SNR when choosing drive field amplitude and frequency. To minimize blurring without sacrificing SNR, a potential scenario may be to pair a low drive field amplitude with a relatively high frequency.

While we have tested multiple drive field frequencies on the relaxometer, MPI scanners are typically designed at a fixed operating frequency but can operate at a range of drive field amplitudes. The operational envelope will be limited due to safety concerns such as peripheral nerve stimulation and specific absorption rate (SAR) [29, 84]. Within the range of clinically safe scanning rates, scanning sequences may be carefully chosen to minimize relaxation effects. Eliminating blur due to relaxation may be an important avenue to improving MPI spatial resolution. Here we observe that a lower drive field amplitude will reduce relaxation-induced blurring, but cause a linear reduction in SNR. Additionally, scanning sequences may be selected to distinguish regions of different relaxation behavior. Measuring relaxation times might also enable biosensor applications such as detecting the binding of a functionalized SPIO to a targeted protein or cell [78, 79].

3.6 Conclusions

In this work, we investigated the drive-field dependence of relaxation-induced blurring in MPI. To do so, we examined nanoparticle relaxation times, phase lag, and resolution at multiple drive field amplitudes and frequencies.

We found that spatial resolution in both the MPI scanner and relaxometer deteriorated with increasing drive field amplitude and was approximately independent of drive field frequency. The image blurring with increasing drive field amplitude was consistent despite measured relaxation times decreasing with both increasing drive field amplitude and frequency. We instead found that expressing the relaxation time constant as a phase lag shows that relaxation can be expressed in a frequency-independent metric, enabling accurate estimations of relaxation-induced blur that are a function of phase lag and drive field amplitude. While increasing drive field amplitude deteriorates resolution, faster scanning gives large SNR gains. This in turn creates a tradeoff between relaxation-induced blurring and SNR. Understanding how drive field amplitude and frequency affect MPI relaxation will give guidance in designing MPI scanning sequences and optimized SPIO nanoparticles to minimize image deteriorating relaxation effects, and in developing techniques to exploit relaxation for biosensor applications.

3.7 Appendix

Substituting Equation 3.12 into Equation 3.9, the non-adiabatic x-space imaging equation is written as:

$$\hat{\rho}(x_s(t)) \approx \hat{\rho}_{\text{adiab}}(x_s(t)) * \frac{1}{v_s \tau} \exp \left[-\frac{x_s(t)}{v_s \tau} \right] u(x_s(t)) \quad (3.18)$$

Equation 3.18 can be translated into the spatial frequency domain using a Fourier transform [69]:

$$P(k) = P_{\text{adiab}}(k) \frac{1}{1 + 2\pi i k v_s \tau} \quad (3.19)$$

where $P(k)$ and $P_{\text{adiab}}(k)$ are the Fourier transforms of $\hat{\rho}(x_s(t))$ and $\hat{\rho}_{\text{adiab}}(x_s(t))$, respectively, and k [1/m] is the spatial frequency variable.

We can identify the relaxation term as a filter in the spatial frequency domain with a transfer function

$$R(v_s k) = \frac{1}{1 + 2\pi i k v_s \tau} \quad (3.20)$$

The 3 dB cutoff frequency of $|R(v_s k)|$ is:

$$k_c = \frac{1}{2\pi v_s \tau} = \frac{G}{2\pi^2 H_{\text{amp}} f_0 \tau} \quad (3.21)$$

Here we observe that as $v_s \tau$ increases, k_c will decrease and the relaxation low-pass filter will attenuate a wider band of spatial frequencies.

Chapter 4

Magneto-Viscous Relaxation in Magnetic Particle Imaging

Magnetic particle imaging (MPI) is an emerging imaging modality that non-invasively localizes a superparamagnetic iron oxide (SPIO) nanoparticle tracer and shows great promise as a safer alternative for angiography. MPI has demonstrated excellent contrast, zero attenuation with depth, and the benefits of using a completely safe contrast agent and no ionizing radiation. A current challenge in MPI is limited spatial resolution caused by a phenomenon called relaxation, which delays the SPIOs' magnetic dipole moments as they track the MPI drive field. Here we experimentally observe that the fundamental relaxation times in MPI vary with the applied magnetic fields, which is not expected for Néel or Brownian relaxation mechanisms. We find that dynamic Langevin modeling provides theoretical predictions that accurately model this intriguing behavior. To investigate an drive field-driven relaxation mechanism in MPI, we solve a dynamic Langevin equation from literature and derive a relaxation time constant from this equation. We term this time constant *magneto-viscous relaxation*. We measure relaxation times in the Berkeley x-space relaxometer to test this relaxation model. Measured relaxation times were consistent with the magneto-viscous relaxation theoretical model. Relaxation times decreased with increasing drive field amplitude and frequency. Measured relaxation delays decreased with increasing SPIO magnetic core size and decreasing SPIO hydrodynamic size. Most notably, the magneto-viscous model predicts that relaxation times will decrease as magnetic slew rate increases, a trend which thermal models such as Néel and Brownian relaxation do not predict. A model of magneto-viscous relaxation in MPI will aid in minimizing relaxation times by guiding SPIO design and MPI scanning sequences.

4.1 Introduction

We aim to investigate an drive field-driven relaxation mechanism for MPI to better understand how drive field parameters contribute to relaxation delays and subsequent image blurring. Exciting theoretical studies have investigated a dynamic Langevin differential equation to describe the rotational motion of an ensemble of SPIOs in response to an external magnetic field. Following the work of [59, 60, 61, 62], we solve this differential equation to

derive an expression for a *magneto-viscous* relaxation time constant. To evaluate this model, we compare expected values of magneto-viscous relaxation times to those measured experimentally. We measure relaxation times at a variety of drive amplitudes and frequencies to thoroughly examine how drive parameters affect relaxation delays. This knowledge may guide the design of SPIOs and MPI scanning sequences to minimize drive field-dependent relaxation effects.

4.2 Magneto-Viscous Relaxation Theory

In Section 1.2.1, we reviewed the thermal relaxation mechanisms, Néel and Brownian relaxation. Brownian relaxation and the simple form of Néel relaxation have no dependence on an applied magnetic field, and even the more complex form of Néel relaxation only includes a *constant* magnetic field term. Here we follow the work of [59, 60, 61, 62] to obtain an drive field-dependent relaxation mechanism, which we refer to as *magneto-viscous relaxation*. We hypothesize that this relaxation model will accurately describe the relaxation phenomenon we observe experimentally.

It is very important to recall that both Néel and Brownian relaxation mechanisms typically model the decay of magnetization following the removal of a polarizing field. These relaxation mechanisms do not account for SPIO relaxation delays that show a dependence on a time-varying magnetic field; however, there is experimental evidence of such external field-dependencies [49, 54, 57]. We aim to investigate the case of relaxation delays that occur when an external magnetic field, such as the drive field in MPI, is present. We will focus on the case of SPIOs which physically rotate to reorient their magnetic dipole moments as the SPIOs used in MPI have relatively large magnetic cores (~ 20 nm magnetic core diameter).

4.2.1 Dynamic Langevin Equation

To investigate SPIO rotational behavior in the presence of a time-varying magnetic field, we chose to follow a dynamic Langevin equation that has been used in several theoretical studies to model the physical rotation of magnetic nanoparticles under the influence of an external magnetic field [59, 60, 61, 62]. We use the scalar form of the Langevin equation presented in [59, 60]:

$$6\eta V_h \dot{\theta}(t) = -\mu_0 M_{\text{sat}} V_m H(t) \sin \theta(t) + \sqrt{12\eta V_h k_B T} \xi(t) \quad (4.1)$$

We have neglected inertial effects, and therefore are left with a sum of the torques acting on the nanoparticles (Figure 4.1). The first term, $6\eta V_h \dot{\theta}(t)$, represents the hydrodynamic viscous resistance to rotation where $\dot{\theta}(t)$ [rad/s] is the angular velocity. The second term is the magnetic torque created by an applied field, $\mu(m \times H(t)) = -\mu_0 M_{\text{sat}} V_m H(t) \sin \theta(t)$, where μ_0 [T·m/A] is the vacuum permeability constant, m [A·m²] is the magnetic dipole moment, and M_{sat} [A/m] is the saturation magnetization of the SPIOs. The applied magnetic field $H(t)$ [A/m] and the angle of the magnetic dipole moment $\theta(t)$ [rad] are both defined in reference to the x-axis. Finally, a thermal noise term represents the random rotations of a

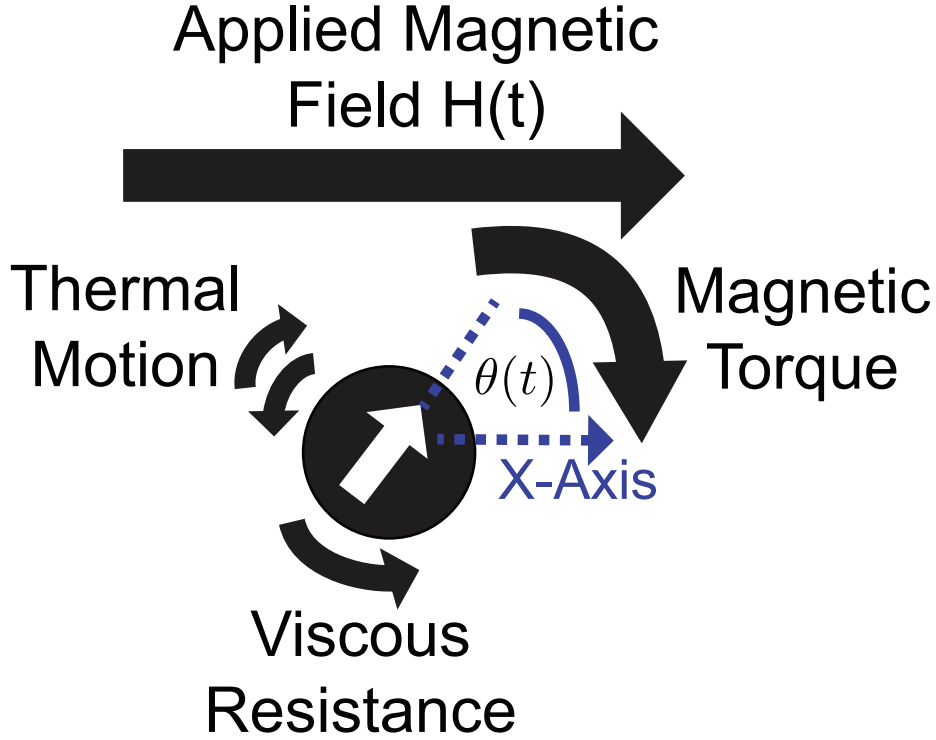


Figure 4.1: SPIO magnetic dipole moment orientation under varying influences where the angle of the magnetic dipole moment $\theta(t)$ and the applied magnetic field $H(t)$ are defined in reference to the x-axis. The applied magnetic field creates a torque on the magnetic dipole moment of the nanoparticle, thermal motion promotes random rotations, and the viscosity of the carrier liquid exerts a resistance against both these motions.

population of nanoparticles, $\sqrt{12\eta V_h k_B T} \xi(t)$, where $\xi(t)$ is a white noise Gaussian random process with zero mean and unit variance.

Here, we want to explore the transient case of SPIO magnetization and dipole orientation, to better understand how SPIO magnetization deviates from the steady-state case described by the Langevin theory of paramagnetism [10]. We aim to describe the case of a SPIO “flip” during a single scan from negative to positive drive field lasting a period of T_s [s], with zero field occurring at time $t = 0$.

For time $t < 0$, the drive field $H(t)$ is negative, and we assume that the SPIO is initially aligned with the field in that direction, $\theta(0) = \pi$, in reference to the x-axis. In this case, $\sin \pi = 0$, making the magnetic torque term as well as the angular velocity term equal to zero. Therefore, the dipole moment will remain aligned with the applied field in stable equilibrium until the drive field changes sign. At time $t = 0$, the direction of the drive field becomes positive and antiparallel to the dipole moment. At this time the dipole moment is in an energetically unfavorable position to rotate. Thermal motion is essential at this time of very low field to perturb the dipole moment from the locked position at $\theta = \pi$. We assume that after some very small time $t = \epsilon$ thermal motion has dispersed the dipole moments from the locked position so that they are free to rotate to align with the drive field. For

time $t \geq \epsilon$ during which the SPIO moments will “flip” to $\theta = 0$, we will assume a small-angle approximation $\sin \theta(t) \cong \theta(t)$. For time $t \geq \epsilon$, the stochastic term $\xi(t)$ has a negligible value compared to the magnetic term; therefore, we will neglect the noise term. Solving for angular velocity we find:

$$\dot{\theta}(t) = \begin{cases} 0 & : t < \epsilon \\ -\alpha H(t)\theta(t) & : t \geq \epsilon \end{cases} \quad (4.2)$$

where we have defined the scalar term: $\alpha = \frac{\mu_0 M_{\text{sat}} V_{\text{m}}}{6\eta V_{\text{h}}} [\text{m}/(\text{A}\cdot\text{s})]$. Using separation of variables, we can find a solution to this differential equation to solve for $\theta(t)$

$$\theta(t) = \begin{cases} \pi & : t < \epsilon \\ \pi \exp \left[-\alpha \int_{\epsilon}^t H(\sigma) d\sigma \right] & : t \geq \epsilon \end{cases} \quad (4.3)$$

4.2.2 Magneto-Viscous Relaxation Time Constant

From [10], the magnetization $M(t)$ [A/m] of an ensemble of N nanoparticles can be calculated as $M(t) = Nm \langle \cos \theta(t) \rangle$, for $t \geq \epsilon$:

$$M(t) = Nm \cos \left(\pi \exp \left[-\alpha \int_{\epsilon}^t H(\sigma) d\sigma \right] \right) \quad (4.4)$$

We solve this equation for various cases of $H(t)$, see Section 4.7.

In this work we seek a relaxation time constant for MPI magnetization. If we assume a single scanning direction in which the FFP traverses a region at constant velocity, we can relate time and FFP position $x_s(t)$ [m] by a simple linear function: $x_s(t) = v_s t$ where v_s [m/s] is the peak FFP velocity and t [s] is time. The drive field $H(t)$ [A/m] of a linear function can be calculated as $H(t) = G x_s(t) = G v_s t$ where G [A/m²] is the magnetic field gradient. Using this approximation for $H(t)$ in Equation 4.4 and assuming ϵ is negligibly small, we obtain:

$$M(t) = Nm \cos \left(\pi \exp \left[-\frac{\alpha G v_s}{2} t^2 \right] \right) \quad (4.5)$$

We can rewrite the exponential term in Equation 4.5 so that it is in the form of a Gaussian function:

$$M(t) = Nm \cos \left(\pi \exp \left[-\frac{\pi t^2}{\tau_{\text{MV}}^2} \right] \right) \quad (4.6)$$

where

$$\tau_{\text{MV}} = \sqrt{\frac{2\pi}{\alpha G v_s}} = \sqrt{\frac{12\pi\eta V_{\text{h}}}{\mu_0 M_{\text{sat}} V_{\text{m}} G v_s}} \quad (4.7)$$

This time constant characterizes the convergence of the magnetization towards the steady-state case. We term this relaxation time constant *magneto-viscous* since it represents the ratio of rotational hydrodynamic resistance to magnetic torque. This contrasts the Brownian relaxation time constant, which is the ratio of rotational hydrodynamic resistance to thermal energy. This equation predicts that increases in viscous resistance, such as increased SPIO hydrodynamic size or viscosity, will increase relaxation time delays. Relaxation times may be reduced by increases in the magnetic torque, such as increased magnetic slew rate of the drive field or increased SPIO magnetic core size. We will test this proposed model for MPI relaxation times by comparing theoretical magneto-viscous relaxation times with experimentally-measured relaxation times from the Berkeley x-space relaxometer.

4.3 Methods

4.3.1 Berkeley X-Space Relaxometer

The Berkeley MPI relaxometer (Figure 3.2) measures the x-space point spread function (PSF) without an imaging gradient and has been described previously in Sections 2.3.2 & 3.3.2 and in [41, 57, 80]. This system is similar in goal to a MPI spectrometer, which measures the spectrum of SPIO magnetization for harmonic reconstruction MPI [70, 71]; however, the relaxometer measures information in the time domain for x-space reconstruction methods. The system scans the virtual FFP with an drive coil and detects the SPIO response via an inductive receive coil.

4.3.2 Linear Approximation for the Time-varying Drive Field

Here we will again assume a linear function to approximate x-space MPI scanning [41] because oscillating drive fields, such as a sinusoid, are linear around the time of zero field. This linear region of the sinusoid is the critical region of scanning, as this is when the FFP passes over and elicits a signal from SPIOs.

Similarly to Section 3.2.2, we calculate magnetic slew rate Gv_s [A/(m·s)] for a sinusoidal drive field $H(t) = H_{amp} \sin(2\pi f_0 t)$ as:

$$Gv_s = 2\pi H_{amp} f_0 \tag{4.8}$$

where H_{amp} [A/m] is the peak amplitude and f_0 [Hz] is the frequency of the drive field. This approximation will help us understand how magnetic slew rate affects MPI relaxation times.

4.3.3 Experimental Relaxation Time Measurements

4.3.3.1 Fitting Algorithm

The fitting algorithm is a nonlinear least-squares optimization method that calculates candidate theoretical signals for various relaxation times and nanoparticle magnetic core size distributions. The experimental and theoretical signals were compared in the gridded image domain at a FOV of 25 mT-pp (peak-to-peak), and the candidate relaxation time τ which

minimized error between the experimental and theoretical signals was determined as the best estimate for relaxation time. This fitting algorithm was performed with single-FOV experimental signals from the relaxometer; the bias coil and partial FOV method were not employed for these measurements. The theoretical signal was calculated for 10 cycles of the drive field and was sampled at 10 MHz. These computations were performed using MATLAB software (Mathworks MATLAB, Natick, MA, USA). This fitting algorithm has been previously demonstrated and described in Section 2.3.4 and in [57, 80].

4.3.3.2 Non-Adiabatic X-Space Theoretical Calculations

Theoretical calculations were used in a fitting scheme with each of the experimental signals acquired in the Berkeley x-space relaxometer. The theoretical signal was calculated using the non-adiabatic x-space theory previously described in Section 2.2.2, which adds relaxation effects to the x-space theory [41]. The non-adiabatic signal was calculated as a temporal convolution of the adiabatic signal with a relaxation term $r(t)$ that describes a relaxation process based on a characteristic relaxation time constant τ ; we previously derived this term as an exponential process, $r(t) = \exp\left[-\frac{t}{\tau}\right]$. Following the convergence process derived in Equation 4.6, we chose here a Gaussian relaxation process $r(t) = \exp\left[-\frac{\pi t^2}{\tau^2}\right]$. The non-adiabatic x-space theoretical MPI signal was calculated as:

$$s(t) = \gamma \left(\dot{x}_s(t) \rho(x) * \dot{\mathcal{L}} \left[\frac{Gx}{H_{\text{sat}}} \right] \Big|_{x=x_s(t)} \right) * r(t) \quad (4.9)$$

$$= \gamma \left(\dot{x}_s(t) \rho(x) * \dot{\mathcal{L}} \left[\frac{Gx}{H_{\text{sat}}} \right] \Big|_{x=x_s(t)} \right) * \exp \left[-\frac{\pi t^2}{\tau^2} \right] \quad (4.10)$$

where $\gamma = \frac{B_1 m G}{H_{\text{sat}}}$ is a scalar term, B_1 [T/A] is the sensitivity of the receive coil, H_{sat} [A/m] measures how easily a SPIO saturates, $\dot{x}_s(t)$ [m/s] is the FFP velocity, $\rho(x)$ [nanoparticles/m] is the 1D SPIO density, and $\mathcal{L}[\bullet]$ is the Langevin function of paramagnetism (not to be confused with the dynamic Langevin equation used previously in Equation 4.1). These theoretical calculations used the same inputs as each relaxometer experiment, such as drive frequency and field amplitude, sampling frequency, etc., and used the mean magnetic core diameter of the SPIOs, as determined by transmission electron microscopy (TEM). The theoretical calculations assumed a log normal distribution of SPIO magnetic core diameters, but a single relaxation time constant τ , which is estimated using the fitting algorithm and therefore not calculated using Equation 4.7.

4.3.4 Magneto-Viscous Relaxation Time Theoretical Calculations

Predicted magneto-viscous relaxation times were calculated according to Equation 4.7 for four samples of SPIOs: Resovist, UW20-A, UW20-B, and UW23. Resovist (Bayer-Schering, Berlin, Germany) is a commercially-manufactured SPIO tracer with a carboxydextran coating developed for MRI [5]. The other three samples were synthesized at the University of Washington (UW) [8, 9, 57].

Magnetic core diameters (D_m) of the UW nanoparticles were measured using ImageJ software (National Institutes of Health) from images acquired using TEM (FEI Tecnai 12) (Table 4.1). As seen in the TEM images in Figure 4.2, the UW nanoparticles are single-domain, and therefore it is straightforward to measure the diameter of the iron oxide core seen in the images. The Resovist nanoparticles, however, are believed to be multi-core nanoparticles in which many smaller nanoparticles are aggregated within the same coating [81, 82]. Therefore, we cannot measure Resovist magnetic core size using TEM images, and instead assumed an effective magnetic core diameter of 17 nm based on our previous relaxometry studies [44, 57, 85]. We measured hydrodynamic diameters (D_h) using dynamic light scattering (DLS) results which were intensity-weighted (Table 4.1); the measured value for Resovist was consistent with reported values in literature [5, 81].

To calculate the magneto-viscous relaxation times, we used a log-normal distribution of magnetic core diameters (Table 4.1). For the hydrodynamic diameters, we did not use the DLS measurements. We ran a nonlinear least squares optimization scheme to select the optimal coating size that produced the best match between the theoretical and experimentally-measured relaxation times, solving for a single coating size across a range of magnetic slew rates. Hydrodynamic diameter distributions were calculated as the magnetic core diameter distribution plus the coating size (Table 4.1). We assumed a saturation magnetization M_{sat} of $0.6 \text{ T}/\mu_0$ for all samples used in this study.

Sample	D_m (nm)		D_h (nm)	
	Measured	Theoretical	Measured	Theoretical
Resovist	N/A	17 ± 2	62.1	19.6 ± 2
UW20-A	20.9 ± 2.3	20 ± 2	79.9	24.3 ± 2
UW20-B	20.0 ± 1.8	20 ± 2	145.2	29.2 ± 2
UW23	23.1 ± 1.6	23 ± 2	88.0	24.5 ± 2

Table 4.1: Magnetic core diameter distributions (mean \pm standard deviation) as measured by transmission electron microscopy (TEM), the magnetic core diameter distributions used in the theoretical calculations of magneto-viscous relaxation times, hydrodynamic diameters as measured by dynamic light scattering (DLS), and the hydrodynamic diameter values used in theoretical calculations of magneto-viscous relaxation times.

4.4 Results

4.4.1 Relaxation Times Decrease with amplitude of Magnetic Torque

4.4.1.1 Relaxation with Magnetic Slew Rate

We compare relaxation times of two nanoparticle samples, Resovist and UW20-A, which were measured over a range of magnetic slew rates (Gv_s) in the Berkeley x-space relaxometer, to predicted values of magneto-viscous relaxation times (Figure 4.3). Relaxation times were measured in the relaxometer at five frequencies (2.3, 4.5, 9.3, 12.2, and 25 kHz) at drive field amplitudes ranging from 15 to 70 mT. We calculated the theoretical magneto-viscous relaxation times using the hydrodynamic diameter distribution that gave the best fit to the experimental data (Table 4.1). For both nanoparticle samples, measured relaxation times decreased with increasing magnetic slew rate (Figure 4.3). This trend was consistent when increasing magnetic slew rate via both drive frequency and field amplitude, and the predicted values for magneto-viscous relaxation times followed a similar trend.

4.4.1.2 Relaxation with Magnetic Size

Relaxation times were measured in the relaxometer at three frequencies (4.4, 9.1, and 11.5 kHz) for an identical range of magnetic slew rate. We averaged the three sets of relaxation times and calculated the standard deviation of the relaxation times between the three frequency sets. The average and standard deviation of the measured relaxation times are displayed and compared to predicted magneto-viscous relaxation times for UW20-A and UW23 in Figure 4.4A. These two nanoparticle samples had different magnetic core volumes but similar hydrodynamic volumes according to TEM and DLS measurements. We calculated the theoretical magneto-viscous relaxation times using the hydrodynamic diameter distribution that gave the best fit to the experimental data, and these two distributions were nearly identical (Table 4.1). As in Section 4.4.1.1, measured relaxation times decreased with increasing magnetic slew rate for both nanoparticle samples, consistent with theoretical predictions. Also consistent with the magneto-viscous theory, the SPIO sample with the larger magnetic core size had consistently faster relaxation times across the range of magnetic slew rates measured.

4.4.2 Relaxation Times Increase with Viscous Resistance

We also compared the measured relaxation times of two nanoparticle samples with the same magnetic volume but different hydrodynamic volumes. The average relaxation times (averaged for three sets of measured relaxation times, each acquired at a different frequency: 4.4, 9.1, and 11.5 kHz), as well as the standard deviations of relaxation times between the three frequency sets, are displayed for each magnetic slew rate and compared to the predicted magneto-viscous relaxation times in Figure 4.4B. Measured relaxation times decreased with increasing magnetic slew rate for both nanoparticle samples, consistent with magneto-viscous theoretical predictions. The SPIO sample with the larger coating size, UW20-B, had much larger relaxation times than UW20-A. The coating size ($D_h - D_m = 9.2$ nm) of UW20-B used to calculate the theoretical magneto-viscous relaxation times was approximately a factor of

2 larger than the coating size ($D_h - D_m = 4.3$ nm) used to calculate UW20-A theoretical relaxation times. This relative change is consistent with that measured by DLS (Table 4.1); the coating size of UW20-B ($D_h - D_m = 124.9$ nm) was measured by DLS to be twice the coating size of UW20-A ($D_h - D_m = 59.0$ nm).

4.5 Discussion

We introduce here the magneto-viscous relaxation mechanism for MPI, which describes the ability of the magnetic torque to physically rotate the nanoparticle against viscous resistance. The stronger the magnetic torque, or the less the viscous resistance, the faster the nanoparticle will follow the drive field with smaller relaxation delay times. The four main variables in this relaxation mechanism are:

- *Magnetic Slew Rate*: Faster drive scanning decreases relaxation times. We demonstrated this effect by increasing the magnetic slew rate of the relaxometer via both drive frequency and field amplitude. This observed variation in relaxation rates with drive parameters is consistent with the magneto-viscous relaxation model but is not consistent with the Néel or Brownian models. The inability of the Néel and Brownian models to accurately describe MPI relaxation behavior should perhaps be expected as these mechanisms model the decay to zero magnetization following the *removal* of a magnetic field.
- *SPIO Magnetic Core Size*: In addition to improving resolution [40, 41], SPIOs with larger magnetic cores have faster relaxation times. The relaxation times of a 23 nm magnetic core SPIO were shorter than those of a 20 nm magnetic core SPIO with a similar coating size. The standard deviations of relaxation times between measured frequencies in Figure 4.4 were larger at low magnetic slew rates due to lower SNR at lower magnetic slew rate. As previously described, SNR scales with magnetic slew rate in MPI [41].
- *SPIO Coating Size*: Relaxation times increase as the polymer coating of the nanoparticle increases in size, which increases the hydrodynamic volumes of the nanoparticle. Doubling the coating size of a 20 nm magnetic core SPIO increased measured relaxation times. Similar to Figure 4.4, the standard deviations of relaxation times between measured frequencies was greater for lower magnetic slew rates due to less SNR.
- *Solvent Viscosity*: As the viscosity of the solvent increases, relaxation times are expected to increase, given that no other variables change. Experimental work by [65, 66] has demonstrated that harmonic ratios of the MPI signal do change with solvent viscosity, and these effects are attributed to increases in relaxation time with increasing solvent viscosity. We are still investigating the role viscosity plays in MPI as polymers such as dextran (Sephadex) and PEG can contract or swell in response to different solvents [86, 87], and this characteristic makes it difficult to isolate the effect of viscosity separately from changes in hydrodynamic volume.

For our theoretical calculations of magneto-viscous relaxation times, we used smaller hydrodynamic diameters than those indicated by DLS measurements. This parameter of our model warrants further exploration. It may be that an *effective* hydrodynamic diameter should be used in these calculations, and this variable may take into consideration the polymer coating’s ability to expand and contract. Although the DLS-measured hydrodynamic sizes were not used to compare theoretical relaxation values to the experimental values, the relative change between the coating sizes of the small coating SPIO versus the large coating SPIO did correspond well with DLS measurements.

Each of the SPIO samples used in this study contain a distribution of nanoparticle sizes. While the mean magnetic core diameter indicates that these SPIO samples are large enough to have locked dipole moments and therefore will physically rotate in the liquid, the dipole moments of the smaller nanoparticles in the distribution may reorient within the magnetic material itself. At the other extreme, the largest nanoparticles in the distribution may be reaching the single-domain size limit and may be ferromagnetic instead of superparamagnetic [88, 89]. While not every nanoparticle in the sample may be experiencing magneto-viscous relaxation, it is the dominant mechanism that characterizes the sample behavior as an ensemble. The UW samples contain distinctly single-domain magnetic cores (Figure 4.2) that are predominantly in the size range of the magneto-viscous mechanism. The characteristics of these nanoparticles fit the magneto-viscous description very well, and our experiments demonstrate that they behave similarly to this model. Resovist is less of an ideal magneto-viscous candidate as it has have a multi-aggregate configuration of clusters of small nanoparticles which are encased together in the polymer coating [5, 81]; however, our Resovist experiments also correlate well with the magneto-viscous model, indicating that this is the dominant relaxation mechanism for Resovist as well.

The magneto-viscous relaxation times may be minimized through two avenues: better SPIO synthesis and faster drive scanning. SPIOs tailored for MPI is a burgeoning area of research which has already demonstrated the critical importance of optimizing SPIO magnetic core size for MPI sensitivity and resolution [8, 67]. This additional knowledge of how magnetic core and coating sizes affect relaxation times can further guide SPIO developers. Designing MPI scanners and scanning sequences that exploit fast scanning will also decrease relaxation times for magneto-viscous-dominated nanoparticles. In addition to enabling the mitigation of relaxation times, understanding magneto-viscous relaxation will also aid us in designing scanner sequences to measure relaxation times. This approach has many molecular and cellular imaging applications; for example, a “color” image of varying relaxation could visualize regions of a functionalized SPIO bound to a targeted protein or cell [78, 79].

4.6 Conclusions

Magneto-viscous relaxation for MPI describes a relaxation mechanism which is dependent on MPI drive field scanning. Measured relaxation times decreased with increasing magnetic slew rate of the Berkeley x-space relaxometer. Faster relaxation times were also achieved by altering SPIO characteristics; increasing SPIO magnetic core size and decreasing SPIO hydrodynamic size decreased measured relaxation times. These experimentally-measured observations correlated well with the theoretical predictions of magneto-viscous relaxation

times. By understanding the factors influencing relaxation times, MPI scientists can design new SPIO constructs and MPI scanning systems to minimize relaxation times or to boost relaxation effects into a source of contrast.

4.7 Appendix

We can solve Equation 4.4 for various cases of $H(t)$ for $t \geq \epsilon$. Again we assume ϵ is negligibly small.

Sinusoidal Drive Field

MPI scanners primarily use a sinusoidal drive field. Substituting $H(t) = H_s \sin(2\pi ft)$ into Equation 4.4, the approximated magnetization equation is:

$$M(t) = Nm \cos \left(\pi \exp \left[-\frac{\alpha H_s}{2\pi f} (1 - \cos [2\pi ft]) \right] \right) \quad (4.11)$$

Linear Drive Field

This case is described in Section 4.2.2, and leads to the derivation of the magneto-viscous relaxation time constant.

Constant Drive Field

Equation 4.4 may also be solved for a constant drive field, $H(t) = H_0$:

$$M(t) = \cos Nm (\pi \exp [-\alpha H_0 t]) \quad (4.12)$$

This form of the equation also lends itself to a characteristic time constant for a convergence process when rewritten as:

$$M(t) = Nm \cos \left(\pi \exp \left[-\frac{t}{\tau_c} \right] \right) \quad (4.13)$$

where

$$\tau_c = \frac{1}{\alpha H_0} = \frac{6\eta V_h}{\mu_0 M_{\text{sat}} V_m H_0} \quad (4.14)$$

This relaxation time constant is similar to the Brownian relaxation time constant, which represents the ratio of viscous resistance to thermal energy. In the case of an external field, the magnetic energy of the applied magnetic field acting on the SPIO is much larger than thermal energy, and we obtain the magnetic energy of the applied magnetic field in the denominator instead. Similar time constants have been derived in the literature [46, 49, 55, 56].

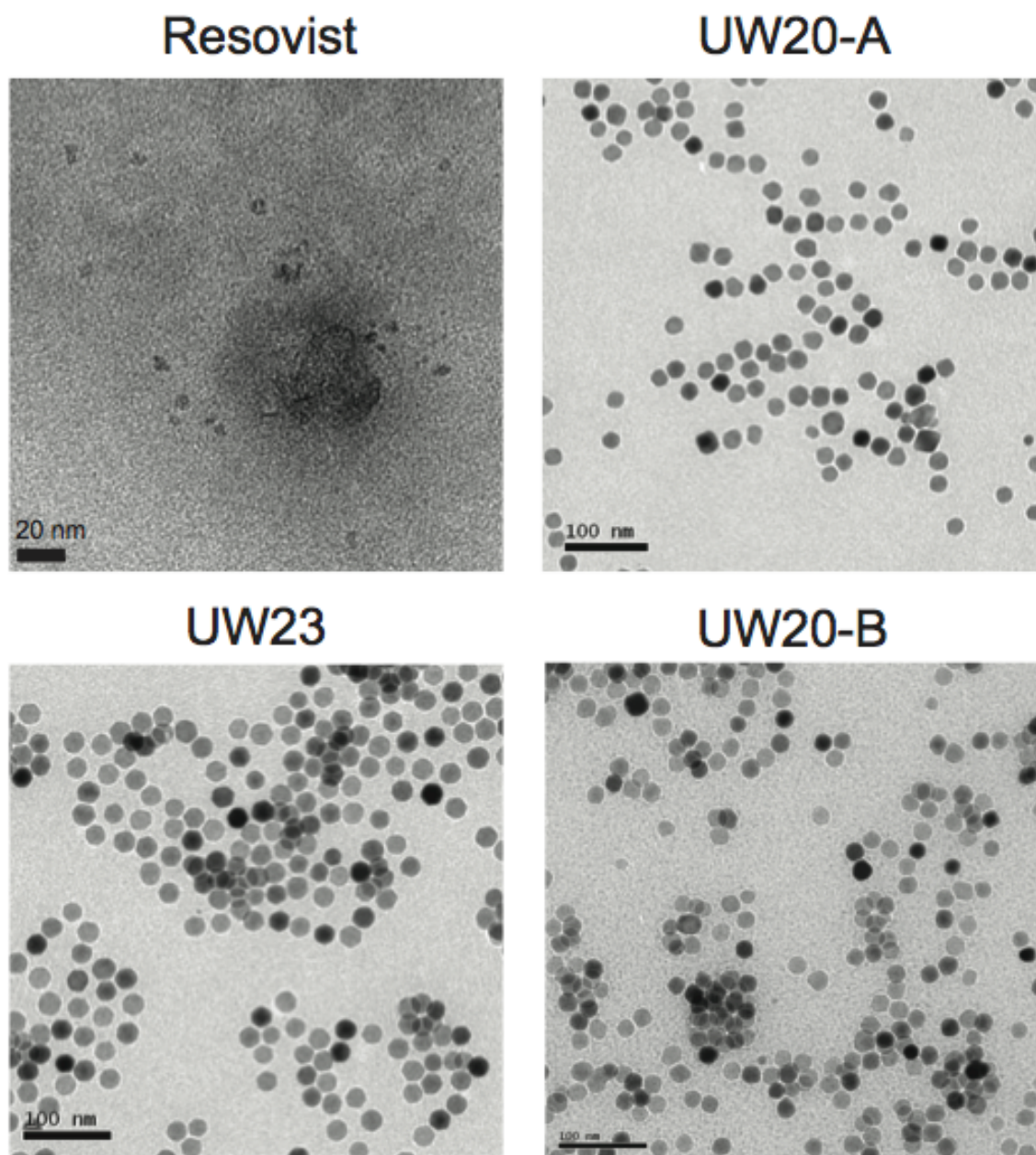


Figure 4.2: Transmission electron microscopy (TEM) images of the SPIO nanoparticle tracers: Resovist and three samples of varying magnetic and hydrodynamic sizes (UW20-A, UW20-B, and UW23) synthesized at the University of Washington.

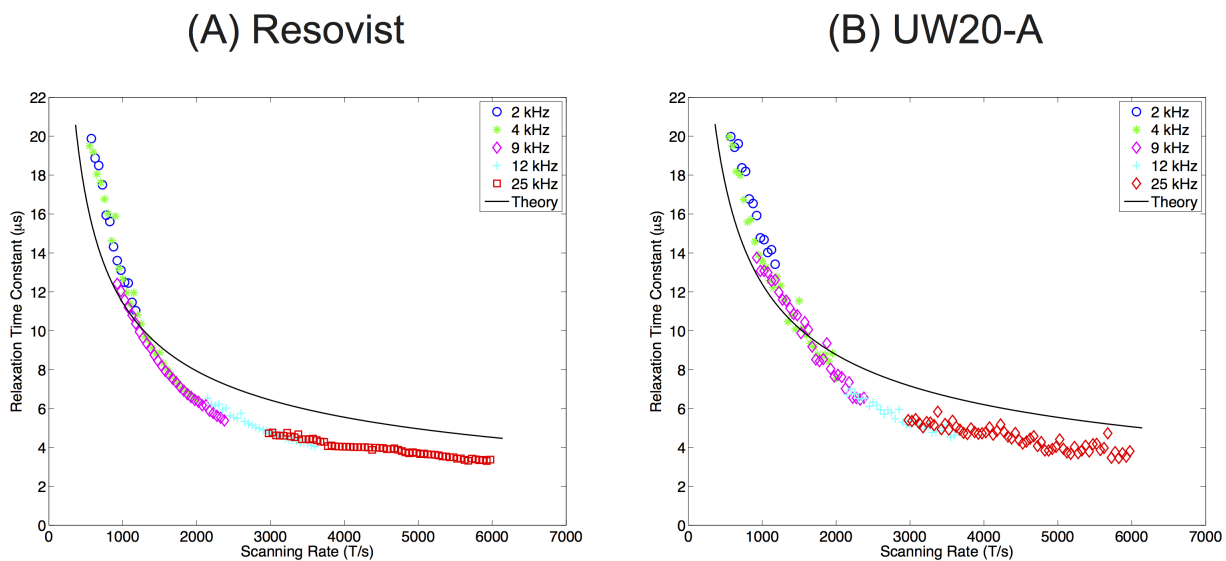


Figure 4.3: Measured relaxation times for Resovist (A) and UW20-A (B) decreased with increasing magnetic slew rate. Relaxation times were acquired in the Berkeley x-space relaxometer at five frequencies (2.3, 4.5, 9.3, 12.2, and 25 kHz) for drive field amplitudes in the range of 15-70 mT. The measured relaxation times compared well with the theoretical values predicted by magneto-viscous relaxation across the range of measured magnetic slew rates.

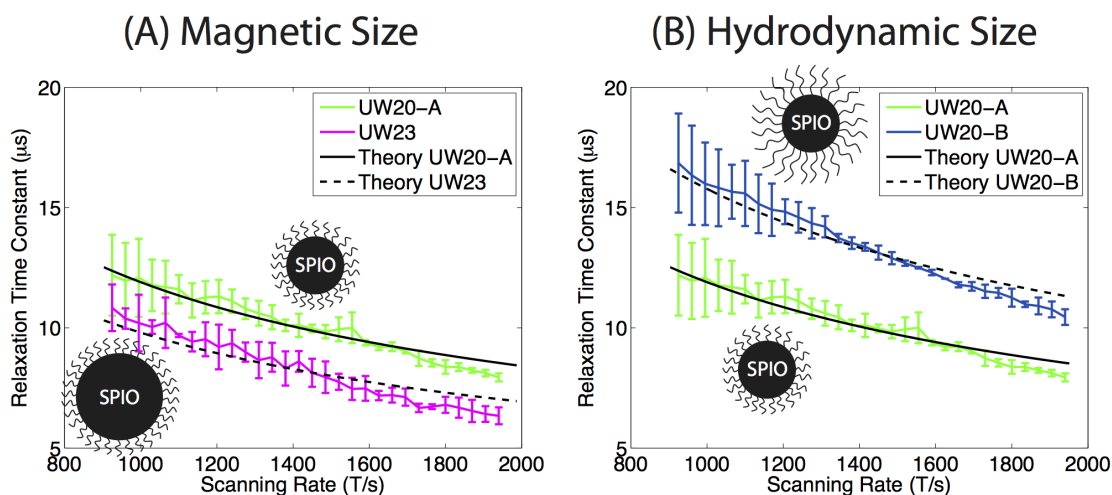


Figure 4.4: Measured and theoretical relaxation times for UW20-A are compared to those for a sample with a larger magnetic size (UW23) and a larger hydrodynamic size (UW20-B). (A) The SPIO sample with a larger magnetic core, UW23, had shorter relaxation times as compared to those of UW20-A, as predicted by magneto-viscous relaxation theoretical calculations. (B) The UW20-B sample had greater relaxation times than UW20-A as predicted by the magneto-viscous relaxation predictions. Experimentally-measured relaxation times were acquired in the Berkeley x-space relaxometer at three frequencies (4.4, 9.1, and 11.5 kHz); the average and standard deviation between the three frequencies are displayed at each magnetic slew rate.

Chapter 5

Future Directions

5.1 Biosensor Applications

MPI is an exciting alternative for studying physiological processes in *in vivo* or clinical settings. Functionalized SPIOs can be used as biosensors to measure serum levels of a desired target such as a protein or other molecule. The binding of functionalized SPIOs to targeted proteins has been demonstrated to increase relaxation times, and possibly allow for quantification of the target [78, 79, 90, 91, 92]. This approach could be useful to measure blood levels of glucose in patients with diabetes, among many other applications.

SPIO biosensor applications can be more complex than a single SPIO binding to a single targeted molecule. Many targeting peptides or antibodies can be conjugated to the SPIO polymer coating, giving that SPIO the ability to bind to many targets. In fact, multiple SPIOs and targets may form a large assembly together (Figure 5.1). The size of the assembly would grow with increased concentrations of the targeted molecule. If the dominant SPIO relaxation mechanism is Brownian or magneto-viscous, relaxation times will increase due to the increasing size of the particle-target assembly. Alternatively, fixation within the assembly may cause the SPIOs to lose the freedom to physically rotate. If the SPIOs are immobilized, their magnetic dipole moments will only be able to rotate within the magnetic core via Néel relaxation. If Néel relaxation was already the fastest relaxation mechanism for that SPIO, there will be no change in MPI signal; otherwise, relaxation times will increase. If the particles are large enough that their magnetic dipole moments are fixed within the magnetic material and unable to experience Néel relaxation, they will no longer be able to contribute signal. Therefore, increased concentrations of the targeted molecule will be observable through increased relaxation times or signal drop-out.

5.2 Relaxation-Based Contrast in MPI

Relaxation enables image contrast when imaging nanoparticles with different relaxation times. In MRI, T_1 and T_2 contrast maps are generated by careful selection of TR and TE in the pulse sequence. Similarly, specially-designed pulse sequences in the MPI scanner can allow for desired relaxation contrast. Differences in SPIO relaxation behavior could indicate areas of SPIO binding or cellular uptake, which would have many applications including

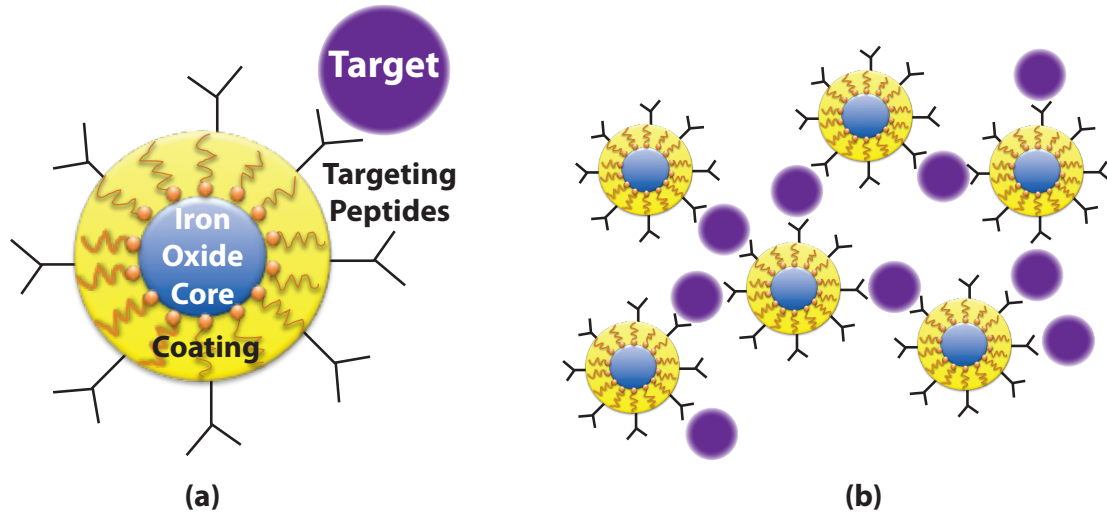


Figure 5.1: Illustration of (a) a functionalized SPIO biosensor and its target, which can form (b) an assembly of multiple SPIOs and targets. Relaxation times would increase as the assembly grows larger with increased concentrations of the targeted molecule.

cell tracking and cancer/atherosclerotic plaque detection.

5.2.1 Preliminary MPI Relaxation-Based Contrast Imaging

Currently MPI provides two types of information: 1) the location of the SPIO contrast agent, and 2) SPIO concentrations. The image is a gradient of black (zero SPIO concentration) to white (maximum SPIO concentration). Signal intensity increases linearly with SPIO concentration, therefore the gradient of white in the image increases linearly with SPIO concentration. By including a fiducial of known SPIO concentration, we can deduce the SPIO concentrations throughout the image. Due to relaxation effects, MPI is capable of providing another dimension of information by adding “color” to the image. We aim to gain information about the differing environments or activities of the SPIOs throughout the image by distinguishing variations in SPIO relaxation times.

SPIO relaxation mechanisms could include Néel and Brownian relaxation mechanisms (Section 1.2.1), which are based on thermal processes, or the recently proposed magneto-viscous relaxation mechanism (Chapter 4). By designing specific pulse sequences to exploit the drive field-dependences of relaxation mechanisms, we aim to distinguish pixels of SPIOs with high relaxation times from those with low relaxation times. These differences in relaxation could be indicative of differences in hydrodynamic volume of the particles [57, 62, 67], in the viscosity of the local environment [62, 65, 67], or particle mobility [51, 57].

In Figure 5.2, we demonstrate the first relaxation contrast image. Resovist, Chemicell, and a mixture of Resovist and Chemicell particles were imaged in the projection MPI scanner (Section 2.3.1). The relaxation times of Resovist particles vary with drive field parameters (Sections 3 & 4), and these times are much longer than those of other SPIO samples. In particular, Chemicell has extremely short relaxation times ($< 1 \mu s$) at all drive field scanning conditions. Using a specific pulse sequence, we obtained the relaxation contrast image which

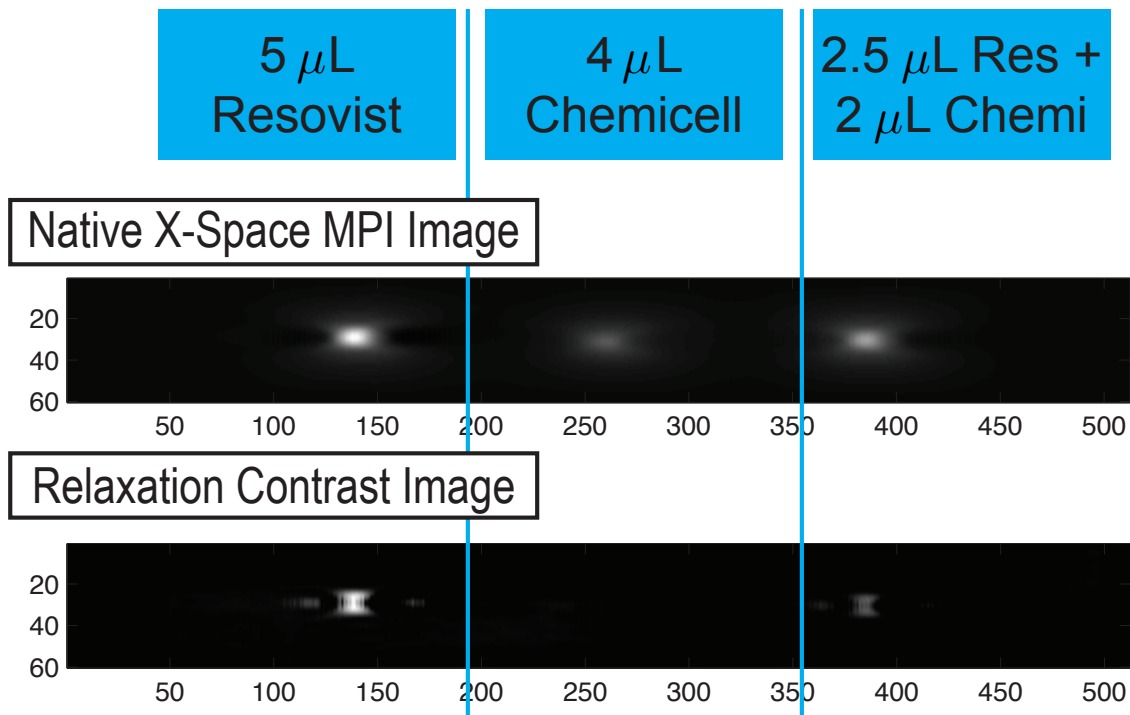


Figure 5.2: The first relaxation-based contrast MPI image distinguishes the SPIOs with longer relaxation times (Resovist); whereas those with short relaxation times (Chemicell) are only seen in the native x-space MPI image.

selectively displays the SPIOs with long relaxation times. The image displays a bright signal for Resovist, no signal for Chemicell, and a less bright signal for the mixture sample, representing the smaller concentration of Resovist. The top image in Figure 5.2 displays the native x-space image of the three samples acquired at a 30 mT drive field amplitude.

5.2.2 Relaxation-Based Contrast Applications

Relaxation-based contrast imaging in MPI would have many applications in pre-clinical and clinical imaging. Figure 5.3 depicts a few potential sources of contrast for these applications. Here we discuss a few of these promising areas of future research in MPI relaxation.

5.2.2.1 Targeted Cancer or Atherosclerotic Plaque Detection

As discussed in Sections 1.1.3.3 & 1.1.3.4, functionalized SPIOs can target a region of interest. SPIOs functionalized with the CREKA peptide bind to clots present both at plaque formation and tumor sites [33, 38], and SPIOs with variants of a RGD peptide target specific integrins present at atherosclerotic plaques and on tumor cells [35, 39]. Using relaxation-based contrast imaging, we can better identify the diseased region by detecting where functionalized SPIOs have bound to a target. When binding occurs, the hydrodynamic diameter of the SPIO may increase or the particle mobility of the SPIO may be hindered. Both of these mechanisms can increase relaxation times. By distinguishing areas of greater relax-

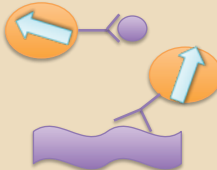


USPIO Binding	Functionalized USPIOs bound to targets will experience longer relaxation times due to increased hydrodynamic size or will experience Néel relaxation due to immobilization	
Viscosity	Relaxation times may increase with viscosity of local environment	
USPIO Cellular Uptake	Relaxation times may alter due to increased viscosity of cellular environment or will experience Néel relaxation due to immobilization	

Figure 5.3: Sources of relaxation-based contrast for MPI

ation, we can differentiate SPIOs bound to diseased targets from other SPIOs present in the image.

A schematic in Figure 5.4 illustrates this concept to diagnose atherosclerotic plaque build-up in the carotid artery (Figure 5.4a). A standard MPI image (5.4b) would show regions of white where SPIOs were present in the bloodstream as well as where SPIOs were localized to the plaque via fibrin-binding or macrophage ingestion. In this image it is difficult to discern the SPIOs located at the plaque from those that are free in the bloodstream. By detecting differences in SPIO relaxation times using relaxation-based contrast (5.4c), the SPIOs present at the plaque are now distinguishable.

5.2.2.2 Visualizing SPIO Uptake at Inflammation Sites

Also discussed in Sections 1.1.3.3 & 1.1.3.4, we may be able to use untargeted approaches to detect tumor margins or atherosclerotic plaques. Phagocytic inflammatory cells such as macrophages uptake the SPIOs at sites of tumors [31, 32] and atherosclerotic plaques [36, 37]. These ingested particles may be immobilized or experience a more viscous intracellular environment as compared to the bloodstream, which would lead to changes in relaxation time. Using relaxation-based contrast, ingested SPIOs at the tumor or plaque could be distinguished from the free SPIOs in the vasculature.

5.2.2.3 Cell Death Monitoring for MPI Cell Tracking

In vivo stem cell tracking is an exciting area of MPI research (Section 1.1.3.2), as MPI is safe, has no depth or penetration limitations, and gives a positive, linear, and quantitative signal with iron concentration. One of the open challenges is how do we ensure that the SPIOs visualized are indeed still tagging a stem cell, or in other words, how do we detect cell death. Labeled stem cells may be tracked more accurately using relaxation-based contrast.

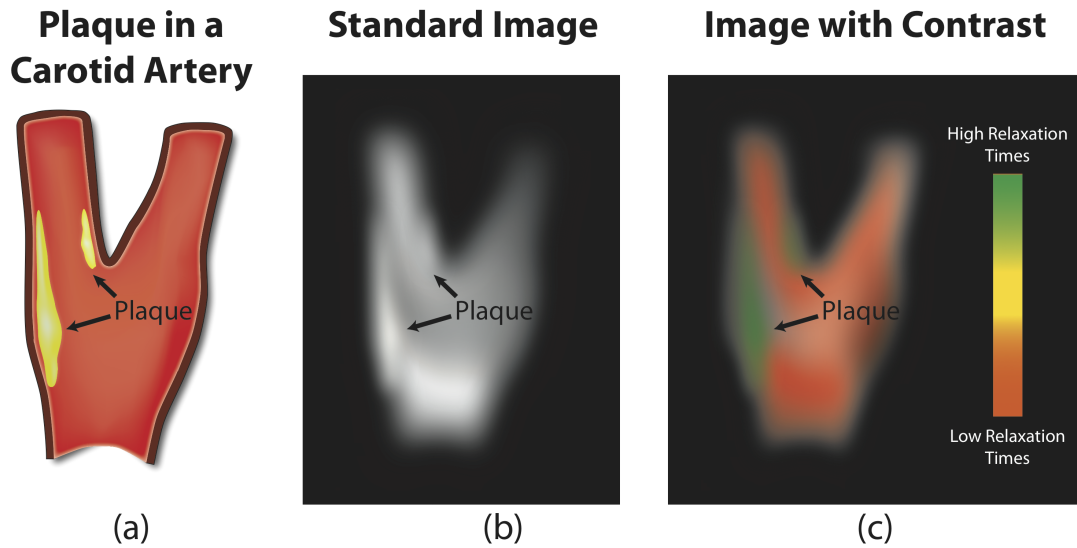


Figure 5.4: Illustrations of (b) a standard MPI image and (c) a relaxation-based contrast image to detect (a) plaque present in the carotid artery. Note that these images are merely illustrations of a concept and are not from data.

Based on the same principles as Section 5.2.2.2, those particles still tagging a cell may have longer relaxation times due to intracellular viscosity or immobilization. This technique would differentiate between SPIOs inside a stem cell from those which are freely circulating after tagged stem cells have lysed.

Chapter 6

Conclusions

This dissertation presents a comprehensive examination of relaxation effects in MPI. We derive theoretical formulations to describe and estimate non-adiabatic imaging, relaxation-induced blurring, and relaxation times. Theoretical predictions are compared to experimentally-measured data acquired in a MPI relaxometer and MPI scanners. Finally, this work gives guidance on how to design SPIOs and MPI scanning sequences to modulate relaxation times and blurring.

The contribution of this work to the field of MPI can be summarized as follows:

- Derivation of the non-adiabatic x-space theory. We demonstrate that the adiabatic x-space theory does not accurately predict the MPI image when moderate relaxation is present. The addition of relaxation effects improves x-space theoretical predictions and demonstrates that relaxation blurs the image in the scanning direction.
- Demonstration of drive field-dependent relaxation-induced blurring. While adiabatic MPI theories predict image resolution to be independent of drive field scanning parameters, we observe variations with drive field for SPIOs of moderate relaxation. We provide a framework for estimating relaxation-induced blur and give experimentally-measured demonstrations of how we can minimize this blur through careful selection of scanning parameters.
- Derivation of the magneto-viscous relaxation mechanism and time constant. For particles with locked dipole moments, we derive a field-driven relaxation mechanism that describes how viscous resistance delays the physical rotation of SPIOs. We demonstrate theoretically and experimentally how magneto-viscous relaxation times can be minimized through SPIO characteristics and drive field parameters.

Relaxation effects will continue to be an important area of MPI research. Image resolution remains a critical challenge for MPI, and minimizing relaxation effects will be an important route to improving resolution, while also potentially improving sensitivity and SNR as well. Relaxation in MPI has the potential for important diagnostic impacts with the development of biosensors and relaxation-based contrast imaging. An improved understanding of relaxation will help motivate the future developments of pulse sequences and SPIOs for MPI.

Bibliography

- [1] B. Gleich and J. Weizenecker. Tomographic imaging using the nonlinear response of magnetic particles. *Nature*, 435(7046):1214–7, 2005.
- [2] J. Weizenecker, B. Gleich, J. Rahmer, H. Dahnke, and J. Borgert. Three-dimensional real-time in vivo magnetic particle imaging. *Physics in Medicine and Biology*, 54(5):L1–L10, 2009.
- [3] P.W. Goodwill, J.J. Konkle, B. Zheng, E.U. Saritas, and S.M. Conolly. Projection X-Space Magnetic Particle Imaging. *Medical Imaging, IEEE*, 31(5):1076–1085, 2012.
- [4] J.J. Konkle, P.W. Goodwill, O.M. Carrasco-Zevallos, and S.M. Conolly. Projection reconstruction magnetic particle imaging. *IEEE Transactions on Medical Imaging*, 32(2):338–47, 2013.
- [5] P. Reimer. Ferucarbotran (Resovist): a new clinically approved RES-specific contrast agent for contrast-enhanced MRI of the liver: properties, clinical development, and. *European Radiology*, 13(6):1266–76, 2003.
- [6] D. Eberbeck, C.L. Dennis, N.F. Huls, K.L. Krycka, C. Grütuner, and F. Westphal. Multicore magnetic nanoparticles for magnetic particle imaging. *IEEE Transactions on Magnetism*, 49(1):269–274, 2013.
- [7] F. Ludwig, T. Wawrzik, T. Yoshida, N. Gehrke, A. Briel, D. Eberbeck, and M. Schilling. Optimization of magnetic nanoparticles for magnetic particle imaging. *IEEE Transactions on Magnetism*, 48(11):3780–3783, 2012.
- [8] R.M. Ferguson, K.R. Minard, A.P. Khandhar, and K.M. Krishnan. Optimizing magnetite nanoparticles for mass sensitivity in magnetic particle imaging. *Medical Physics*, 38(3):1619, 2011.
- [9] K.M. Krishnan. Biomedical nanomagnetism: a spin through possibilities in imaging, diagnostics, and therapy. *IEEE Transactions on Magnetism*, 46(7):2523–2558, 2010.
- [10] N.A. Spaldin. *Magnetic Materials Fundamentals and Applications*. Cambridge University Press, Cambridge, UK, 2003.
- [11] Y. Okuhata. Delivery of diagnostic agents for magnetic resonance imaging. *Advanced Drug Delivery Reviews*, 37(1-3):121–137, 1999.

- [12] G. Dangas, I. Iakovou, E. Nikolsky, E.D. Aymong, G.S. Mintz, N.N. Kipshidze, A.J. Lansky, I. Moussa, G.W. Stone, J.W. Moses, M.B. Leon, and R. Mehran. Contrast-induced nephropathy after percutaneous coronary interventions in relation to chronic kidney disease and hemodynamic variables. *The American Journal of Cardiology*, 95:13–19, 2005.
- [13] P.A. McCullough. Contrast-induced acute kidney injury. *Journal of the American College of Cardiology*, 51(15):1419–1428, 2008.
- [14] P.H. Kuo, Em. Kanal, A.K. Abu-Alfa, and S.E. Cowper. Gadolinium-based MR contrast agents and nephrogenic systemic fibrosis. *Radiology*, 242(3):647–649, 2007.
- [15] J.T. Ferrucci and D.D. Stark. Iron oxide-enhanced MR imaging of the liver and spleen: review of the first 5 years. *American Journal of Roentgenology*, 155(5):943–950, 1990.
- [16] R. Weissleder, D.D. Stark, B.L. Engelstad, B.R. Bacon, C.C. Compton, D.L. White, P. Jacobs, and J. Lewis. Superparamagnetic iron oxide: pharmacokinetics and toxicity. *American Journal of Roentgenology*, 152(1):167–173, 1989.
- [17] M. Lu, M.H. Cohen, S. Rieves, and R. Pazdur. FDA report: Ferumoxytol for intravenous iron therapy in adult patients with chronic kidney disease. *American journal of hematology*, 85(5):315–9, 2010.
- [18] J.F. Schenck. The role of magnetic susceptibility in magnetic resonance imaging: MRI magnetic compatibility of the first and second kinds. *Medical Physics*, 23:815–850, 1996.
- [19] S. Gabriel, R.W. Lau, and C. Gabriel. The dielectric properties of biological tissues: III. Parametric models for the dielectric spectrum of tissues. *Physics in Medicine and Biology*, 41(11):2271–93, 1996.
- [20] P. Röschmann. Radiofrequency penetration and absorption in the human body: limitations to high-field whole-body nuclear magnetic resonance imaging. *Medical Physics*, 14(6):922–931, 1987.
- [21] B. Zheng, T. Vazin, W. Yang, L. Croft, E. Saritas, P. Goodwill, Schaffer D., and S. Conolly. Magnetic particle imaging: a new quantitative cell tracking technique. In preparation.
- [22] J.H. Ix, N. Mercado, M.G. Shlipak, P. Lemos, E. Boersma, W. Lindeboom, W.W. O’Neill, W. Wijns, and P.W. Serruys. Association of chronic kidney disease with clinical outcomes after coronary revascularization: the Arterial Revascularization Therapies Study (ARTS). *American Heart Journal*, 149(3):512–9, 2005.
- [23] D.N. Reddan. Chronic kidney disease, mortality, and treatment strategies among patients with clinically significant coronary artery disease. *Journal of the American Society of Nephrology*, 14(9):2373–2380, 2003.

- [24] J. Coresh, E. Selvin, L.A. Stevens, J. Manzi, J.W. Kusek, P. Eggers, F. Van Lente, and A.S. Levey. Prevalence of chronic kidney disease in the United States. *The Journal of the American Medical Association*, 298(17):2038–47, 2007.
- [25] Vincent F M Segers and Richard T Lee. Stem-cell therapy for cardiac disease. *Nature*, 451:937–42, 2008.
- [26] K.J. Godfrey, B. Mathew, J.C. Bulman, O. Shah, S. Clement, and G.I. Gallicano. Stem cell-based treatments for Type 1 diabetes mellitus: bone marrow, embryonic, hepatic, pancreatic and induced pluripotent stem cells. *Diabetic Medicine*, 29(1):14–23, 2012.
- [27] J.S. Lunn, S.A. Sakowski, J. Hur, and E.L. Feldman. Stem cell technology for neurodegenerative diseases. *Annals of Neurology*, 70(3):353–61, 2011.
- [28] A.S. Arbab, G.T. Yocum, H. Kalish, E.K. Jordan, S.A. Anderson, A.Y. Khakoo, E.J. Read, and J.A. Frank. Efficient magnetic cell labeling with protamine sulfate complexed to ferumoxides for cellular MRI. *Blood*, 104(4):1217–23, 2004.
- [29] E.U. Saritas, P.W. Goodwill, L.R. Croft, J.J. Konkle, K. Lu, B. Zheng, and S.M. Conolly. Magnetic particle imaging (MPI) for NMR and MRI researchers. *Journal of Magnetic Resonance*, In Press., 2013.
- [30] H. Maeda. The enhanced permeability and retention (EPR) effect in tumor vasculature: the key role of tumor-selective macromolecular drug targeting. *Advances in Enzyme Regulation*, 41:189–207, 2001.
- [31] P. Varallyay, G. Nesbit, L.L. Muldoon, R.R. Nixon, J. Delashaw, J.I. Cohen, A. Petrillo, D. Rink, and E.A. Neuwelt. Comparison of two superparamagnetic viral-sized iron oxide particles ferumoxides and ferumoxtran-10 with a gadolinium chelate in imaging intracranial tumors. *American Journal of Neuroradiology*, 23(4):510–9, 2002.
- [32] E.A. Neuwelt, P. Várallyay, A.G. Bagó, L.L. Muldoon, G. Nesbit, and R. Nixon. Imaging of iron oxide nanoparticles by MR and light microscopy in patients with malignant brain tumours. *Neuropathology and Applied Neurobiology*, 30(5):456–71, 2004.
- [33] D. Simberg, T. Duza, J.H. Park, M. Essler, J. Pilch, L. Zhang, A.M. Derfus, M. Yang, R.M. Hoffman, S. Bhatia, M.J. Sailor, and E. Ruoslahti. Biomimetic amplification of nanoparticle homing to tumors. *Proceedings of the National Academy of Sciences of the United States of America*, 104(3):932–6, January 2007.
- [34] J.H. Park, G. von Maltzahn, L. Zhang, A.M. Derfus, D. Simberg, T.J. Harris, E. Ruoslahti, S.N. Bhatia, and M.J. Sailor. Systematic surface engineering of magnetic nanoworms for in vivo tumor targeting. *Small*, 5(6):694–700, 2009.
- [35] K.N. Sugahara, T. Teesalu, P.P. Karmali, V.R. Kotamraju, L. Agemy, O.M. Girard, D. Hanahan, R.F. Mattrey, and E. Ruoslahti. Tissue-penetrating delivery of compounds and nanoparticles into tumors. *Cancer Cell*, 16(6):510–20, 2009.

- [36] M.E. Kooi, V.C. Cappendijk, K.B.J.M. Cleutjens, A.G.H. Kessels, P.J.E.H.M. Kitslaar, M. Borgers, P.M. Frederik, M.J.A.P. Daemen, and J.M.A. van Engelshoven. Accumulation of ultrasmall superparamagnetic particles of iron oxide in human atherosclerotic plaques can be detected by in vivo magnetic resonance imaging. *Circulation*, 107(19):2453–8, 2003.
- [37] S.A. Schmitz, M. Taupitz, S. Wagner, K.J. Wolf, D. Beyersdorff, and B. Hamm. Magnetic resonance imaging of atherosclerotic plaques using superparamagnetic iron oxide particles. *Journal of Magnetic Resonance Imaging*, 14(4):355–61, 2001.
- [38] D. Peters, M. Kastantin, V.R. Kotamraju, P.P. Karmali, K. Gujraty, M. Tirrell, and E. Ruoslahti. Targeting atherosclerosis by using modular, multifunctional micelles. *Proceedings of the National Academy of Sciences of the United States of America*, 106(24):9815–9, 2009.
- [39] L.O. Johansson, A. Bjørnerud, H.K. Ahlström, D.L. Ladd, and D.K. Fujii. A targeted contrast agent for magnetic resonance imaging of thrombus: implications of spatial resolution. *Journal of Magnetic Resonance Imaging*, 13(4):615–8, 2001.
- [40] J. Rahmer, J. Weizenecker, B. Gleich, and J. Borgert. Signal encoding in magnetic particle imaging: properties of the system function. *BMC Medical Imaging*, 9(1):4, 2009.
- [41] P.W. Goodwill and S.M. Conolly. The x-space formulation of the magnetic particle imaging process : 1-D signal, resolution, bandwidth, SNR, SAR, and magnetostimulation. *IEEE Transactions on Medical Imaging*, 29(11):1851–1859, 2010.
- [42] P.W. Goodwill and S.M. Conolly. Multidimensional x-space magnetic particle imaging. *IEEE Transactions on Medical Imaging*, 30(9):1581–1590, 2011.
- [43] K. Lu, P.W. Goodwill, E.U. Saritas, B. Zheng, and S.M. Conolly. Linearity and shift-invariance for quantitative magnetic particle imaging. *IEEE Transactions on Medical Imaging*, DOI: 10.1109/TMI.2013.2257177, 2013.
- [44] P.W. Goodwill, K. Lu, B. Zheng, and S.M. Conolly. An x-space magnetic particle imaging scanner. *Review of Scientific Instruments*, 83:033708, 2012.
- [45] R.E. Rosensweig. Magnetic fluids. *Annual Review of Fluid Mechanics*, 19(1):437–461, 1987.
- [46] M.I. Shliomis. Magnetic fluids. *Soviet Physics-Uspokhi*, 17(2):153–169, 1974.
- [47] L. Néel. Théorie du traînage magnétique des ferromagnétiques en grains fins avec applications aux terres cuites. *Annales de Géophysique*, 5:99–136, 1949.
- [48] W.F. Brown. Thermal fluctuations of a single-domain particle. *Physical Review*, 130(5):1677–1686, 1963.

- [49] S. Neveu-Prin, F.A. Tourinho, J.C. Bacri, and R. Perzynski. Magnetic birefringence of cobalt ferrite ferrofluids. *Colloids and Surfaces A: Physicochemical and Engineering Aspects*, 80(1):1–10, 1993.
- [50] W. Moller, S. Takenaka, N. Buske, K. Felten, and J. Heyder. Relaxation of ferromagnetic nanoparticles in macrophages: In vitro and in vivo studies. *Journal of Magnetism and Magnetic Materials*, 293(1):245–251, 2005.
- [51] R. Kötzitz, P.C. Fannin, and L. Trahms. Time domain study of Brownian and Néel relaxation in ferrofluids. *Journal of Magnetism and Magnetic Materials*, 149(1):42–46, 1995.
- [52] P. Debye. *Polar Molecules*. The Chemical Catalog Company, New York, 1929.
- [53] M.I. Shliomis. Nonlinear effects in suspension of ferromagnetic particles under action of a rotating magnetic field. *Soviet Physics, Doklady*, 19:686–687, 1975.
- [54] J. Dieckhoff, M. Schilling, and F. Ludwig. Fluxgate based detection of magnetic nanoparticle dynamics in a rotating magnetic field. *Applied Physics Letters*, 99(11):112501, 2011.
- [55] T. Yoshida and K. Enpuku. Simulation and quantitative clarification of ac susceptibility of magnetic fluid in nonlinear brownian relaxation region. *Japanese Journal of Applied Physics*, 48(12):127002, 2009.
- [56] C. Caizer. The effect of the external magnetic field on the thermal relaxation of magnetization in systems of aligned nanoparticles. *Journal of Physics: Condensed Matter*, 17(12):2019–2034, 2005.
- [57] P.W. Goodwill, A. Tamrazian, L.R. Croft, C.D. Lu, E.M. Johnson, R. Pidaparathi, R.M. Ferguson, A.P. Khandhar, K.M. Krishnan, and S.M. Conolly. Ferrohydrodynamic relaxometry for magnetic particle imaging. *Applied Physics Letters*, 98(26):262502, 2011.
- [58] A.M. Rauwerdink and J.B. Weaver. Harmonic phase angle as a concentration-independent measure of nanoparticle dynamics. *Medical Physics*, 37(6):2587, 2010.
- [59] A. Engel and P. Reimann. Thermal ratchet effects in ferrofluids. *Physical Review E*, 70(5):051107, 2004.
- [60] M. Raible and A. Engel. Langevin equation for the rotation of a magnetic particle. *Applied Organometallic Chemistry*, 18(10):536–541, 2004.
- [61] J. Weizenecker, B. Gleich, J. Rahmer, and J. Borgert. Particle dynamics of mono-domain particles in magnetic particle imaging. In *Proceedings of the First International Workshop on Magnetic Particle Imaging*, pages 3–15, 2010.
- [62] J.H. Sanchez and C. Rinaldi. Rotational Brownian dynamics simulations of non-interacting magnetized ellipsoidal particles in dc and ac magnetic fields. *Journal of Magnetism and Magnetic Materials*, 321:2985–2991, 2009.

- [63] A.M. Rauwerdink and J.B. Weaver. Harmonic phase angle as a concentration-independent measure of nanoparticle dynamics. *Medical Physics*, 37(6):2587, 2010.
- [64] A.M. Rauwerdink, E.W. Hansen, and J.B. Weaver. Nanoparticle temperature estimation in combined ac and dc magnetic fields. *Physics in medicine and biology*, 54(19):L51–5, 2009.
- [65] A.M. Rauwerdink and J.B. Weaver. Viscous effects on nanoparticle magnetization harmonics. *Journal of Magnetism and Magnetic Materials*, 322(6):609–613, 2010.
- [66] J.B. Weaver and E. Kuehlert. Measurement of magnetic nanoparticle relaxation time. *Medical Physics*, 39(5):2765–70, 2012.
- [67] R.M. Ferguson, K.R. Minard, and K.M. Krishnan. Optimization of nanoparticle core size for magnetic particle imaging. *Journal of Magnetism and Magnetic Materials*, 321(10):1548–1551, 2009.
- [68] D.I. Hoult and R.E. Richards. The signal-to-noise ratio of the nuclear magnetic resonance experiment. *Journal of Magnetic Resonance*, 24:71–85, 1976.
- [69] R.N. Bracewell. *The Fourier Transform and its Applications*. McGraw-Hill, New York, third edition, 2000.
- [70] S. Biederer, T. Knopp, T.F. Sattel, K. Lüdtke-Buzug, B. Gleich, J. Weizenecker, J. Borgert, and T.M. Buzug. Magnetization response spectroscopy of superparamagnetic nanoparticles for magnetic particle imaging. *Journal of Physics D: Applied Physics*, 42(20):205007, October 2009.
- [71] S. Biederer, T.F. Sattel, T. Knopp, L. LaConte, B. Gleich, J. Weizenecker, J. Borgert, and T.M. Buzug. A spectrometer for magnetic particle imaging. In *4th European Conference of the International Federation for Medical and Biological Engineering*, pages 2313–2316. Springer, 2009.
- [72] B. Gleich, J. Weizenecker, H. Timminger, C. Bontus, I. Schmale, J. Rahmer, J. Schmidt, J. Kanzenbach, and J. Borgert. Fast MPI demonstrator with enlarged field of view. In *Proceedings of the International Society for Magnetic Resonance in Medicine*, volume 18, page 218, 2010.
- [73] J. Rahmer, B. Gleich, C. Bontus, I. Schmale, J. Schmidt, J. Kanzenbach, O. Woywode, J. Weizenecker, and J. Borgert. Rapid 3D in vivo magnetic particle imaging with a large field of view. In *Proceedings of the International Society for Magnetic Resonance in Medicine*, volume 19, page 3285, 2011.
- [74] I. Schmale, J. Rahmer, B. Gleich, J. Kanzenbach, J.D. Schmidt, C. Bontus, J. Borgert, and O. Woywode. First phantom and in vivo MPI images with an extended field of view. In *Proceedings of SPIE*, volume 7965, page 796510, 2011.

- [75] K. Lu, P. Goodwill, B. Zheng, and S. Conolly. The impact of filtering direct-feedthrough on the x-space theory of magnetic particle imaging. In *Proceedings of SPIE*, volume 7965, page 79652I, 2011.
- [76] W. Houston. A compound interferometer for fine structure work. *Physical Review*, 29:478–484, 1927.
- [77] M. Shahram. Imaging below the diffraction limit: a statistical analysis. *IEEE Transactions on Image Processing*, 13(5):677–689, 2004.
- [78] R. Kötzitz, W. Weitschies, L. Trahms, W. Brewer, and W. Semmler. Determination of the binding reaction between avidin and biotin by relaxation measurements of magnetic nanoparticles. *Journal of Magnetism and Magnetic Materials*, 194:62–68, 1999.
- [79] A.M. Rauwerdink and J.B. Weaver. Measurement of molecular binding using the Brownian motion of magnetic nanoparticle probes. *Applied Physics Letters*, 96(3):033702, 2010.
- [80] L.R. Croft, P.W. Goodwill, and S.M. Conolly. Relaxation in X-Space Magnetic Particle Imaging. *IEEE Transactions on Medical Imaging*, 31:2335–2342, 2012.
- [81] A.F. Thünemann, S. Rolf, P. Knappe, and S. Weidner. In situ analysis of a bimodal size distribution of superparamagnetic nanoparticles. *Analytical Chemistry*, 81(1):296–301, 2009.
- [82] T. Yoshida, K. Enpuku, F. Ludwig, J. Dieckhoff, T. Wawrzik, A. Lak, and M. Schilling. Characterization of Resovist[®] nanoparticles for magnetic particle imaging. In T.M. Buzug and J. Borgert, editors, *Magnetic Particle Imaging*. Springer Proceedings in Physics, Lübeck, Germany, 2012.
- [83] J. Rahmer, J. Weizenecker, B. Gleich, and J. Borgert. Analysis of a 3D system function measured for magnetic particle imaging. *IEEE Transactions on Medical Imaging*, 31(6):1289–99, 2012.
- [84] E.U. Saritas, P.W. Goodwill, , G.Z. Zhang, and S.M. Conolly. Magnetostimulation limits in magnetic particle imaging. *IEEE Transactions on Medical Imaging*, DOI: 10.1109/TMI.2013.2260764, 2013.
- [85] L.R. Croft, P. Goodwill, A. Tamrazian, K. Krishnan, and S. Conolly. The x-space formulation of magnetic particle imaging including non-negligible relaxation effects. In *Proceedings of SPIE*, volume 7965, page 79652L, 2011.
- [86] T. Ito, M. Yamazaki, and S. Ohnishi. Poly(ethylene glycol)-induced shrinkage of Sephadex gel. *Biophysical Journal*, 56:707–711, 1989.
- [87] E. Antoniou, E. Themistou, B. Sarkar, M. Tsianou, and P. Alexandridis. Structure and dynamics of dextran in binary mixtures of a good and a bad solvent. *Colloid and Polymer Science*, 288(12-13):1301–1312, 2010.

- [88] D.J. Dunlop. Magnetite behavior near the single-domain threshold. *Science*, 176(4030):41–43, 1972.
- [89] D.J. Dunlop. Superparamagnetic and single-domain threshold sizes in magnetite. *Journal of Geophysical Research*, 78(11):1780–1793, 1973.
- [90] A. Astalan, F. Ahrentorp, C. Johansson, K. Larsson, and A. Krozer. Biomolecular reactions studied using changes in Brownian rotation dynamics of magnetic particles. *Biosensors and Bioelectronics*, 19(8):945–951, 2004.
- [91] J.M. Perez, L. Josephson, T. O’Loughlin, D. Högemann, and R. Weissleder. Magnetic relaxation switches capable of sensing molecular interactions. *Nature Biotechnology*, 20(8):816–20, 2002.
- [92] J.M. Perez, F.J. Simeone, Y. Saeki, L. Josephson, and R. Weissleder. Viral-induced self-assembly of magnetic nanoparticles allows the detection of viral particles in biological media. *Journal of the American Chemical Society*, 125(34):10192–3, 2003.